國立臺灣大學電機資訊學院電機工程學研究所

碩士論文

Graduate Institute of Electrical Engineering

College of Electrical Engineering and Computer Science

National Taiwan University

Master Thesis

新型電磁致動與減震之三自由度撓摺結構精密定位平台

A Novel Electromagnetic Actuated and Damped 3-DOF Precision
Positioning Stage with Flexure Suspension

林志憲

Chih-Hsien Lin

指導教授：傅立成 博士

共同指導：陳美勇 博士

Advisor: Li-Chen Fu, Ph.D.

Mei-Yung Chen, Ph.D.

中華民國九十七年六月

June, 2008

致　謝

　　寫了又刪，刪完再重寫，等待了很久的寫致謝的這天，卻又好像什麼也寫不出來。在台大的這兩年，跟各位師長的相處，和實驗室許多學長與同儕之間的回憶，又怎是這一頁就能道盡的。

　　感謝我的指導老師傅立成教授，在這兩年的研究生生涯，您對我的影響不可言喻，老師對理論的嚴謹、對研究的熱忱，我會永遠記在心中。感謝口試委員顏家鈺教授、胡竹生教授、陳永耀教授以及劉昌煥教授，對我的論文提供寶貴的意見，使得內容更加完整。

　　感謝亦師亦友的美勇、勤鎰和紹剛學長，你們對我研究上的指點，是我得以完成這份論文的基石；感謝正民、明理、智富和聖化學長，你們不管上是在學業上、實驗室生活上都是我最好的學長，你們在實驗室的時候會讓我特別安心；感謝銘全和定國學長，在我有過迷惘的時候，是學長們適時地拉了我一把；感謝威文、政昌、國宏和俊緯學長，你們總是給我一些不同的想法來面對事情。

　　感謝怡孜跟琬琳，不僅是在研究跟課業上幫我許多，也在我人生低潮的時候適時鼓勵我；感謝顯真，你將自行車帶入我的生命，讓我的生活得以豐富，難以用言語表達我的感謝；感謝貫豪跟晏榆，這兩年和你們相處很有趣；感謝實驗室的學弟妹們，繕琮、世勳、羿如、柏男、柏徐、志鵬和孟勳，有你們的實驗室總是充滿著歡樂；感謝助理郁璇、懿萱、小寧跟立婷，妳們在行政上面真的幫我太多忙了。

　　感謝我的家人，特別是我的母親，您在最後這段時間忍受我的任性，包容我的不成熟。我永遠都以能生為妳的兒子而感到幸運。

志憲

於電二 236 實驗室

2008.07.25

摘要

本論文提出一種以電磁力產生驅動與減低結構振動的平面式定位平台，可用於精密定位相關應用。平台本體採用一體成型之平行撓性結構做為導引機構，其運動來自結構本身的彈性變型。藉著一個近似均勻強度的磁場與四組線圈，本論文提出一種線性電磁制動器的設計，做為提供驅動平台移動與轉動的力量來源。為了減輕撓性結構天生的共振問題，亦提出了以渦電流效應提高系統阻尼的電磁式阻尼器，其非接觸式的特性較一般接觸式的阻尼器更適合用於本論文所訴求之精密運動控制系統。本新型精密定位平臺達成三大目標：第一，擁有大移動行程的能力（此指公釐的範疇）；第二，精密定位的能力；第三，採用簡潔的機構設計。

為了要在系統參數變化與外在擾動干擾下達到系統穩定與強健性的目標，本論文提出一個強健適應性滑動模式控制器，提升系統在定位與循跡需求上的效能。控制器包含具有強健性的滑動模式控制器，與線上估測系統參數同時調變控制器的適應律。本論文設計的平台最大行程可達到 $3\text{x}3\text{mm}^2$，定位解析度為 $10\mu\text{m}$。透過在時域與頻域上的分析，撓性結構的共振現象可以有效地被渦電流阻尼器減輕。實驗結果亦證實本論文所設計之平面精密定位平台具有所訴求之精密定位與循跡之能力。

關鍵字：精密運動控制，結構減震，平行式撓性機構，電磁制動器，渦電流阻尼器，適應性滑動模式控制

Abstract

This thesis proposes a novel planar electromagnetic actuated and damped positioning stage for precision positioning applications. The moving stage is suspended by the monolithic parallel flexure mechanism, whose motion comes from the elastic deformation of the flexure. A linear electromagnetic actuator which consists of a near-uniform magnetic field and four coils is designed and implemented to provide the propelling force and torque for 3-DOF motions. In order to suppress the vibration of the flexure suspension mechanism, an eddy current damper is designed and integrated with the electromagnetic actuator. Since the electromagnetic damper experiences no contact, it is obviously more adequate than other kinds of contact damper to be incorporated into precision motion control. The three salient features of the novel system design in the research include: (1) to have large moving range (in *mm* level), (2) to achieve precision positioning, and (3) to design a compact mechanism.

For the purpose of gaining system robustness and stability, a robust adaptive sliding-mode controller is proposed to enhance the system performance for both regulation and tracking tasks. The developed robust adaptive control architecture consists of two components: 1) sliding mode controller, and 2) robust adaptive law. With the designed controller, the stage can achieve high positioning resolution, where

the tracking error in each axis is kept within 10μm. Experiment results show the vibration of the flexure mechanism can be suppressed by the eddy current damper successfully in a series of time-domain and frequency domain tests. Besides, the designed traveling range of the positioning stage is 3mm x 3mm in planar motion, and tracking and contouring performance are also examined to assure the appealing dynamic property of the stage.

Keywords: Precision motion control, Vibration suppression, Parallel flexure mechanism, Electromagnetic actuation, Eddy current damper, Adaptive sliding mode control
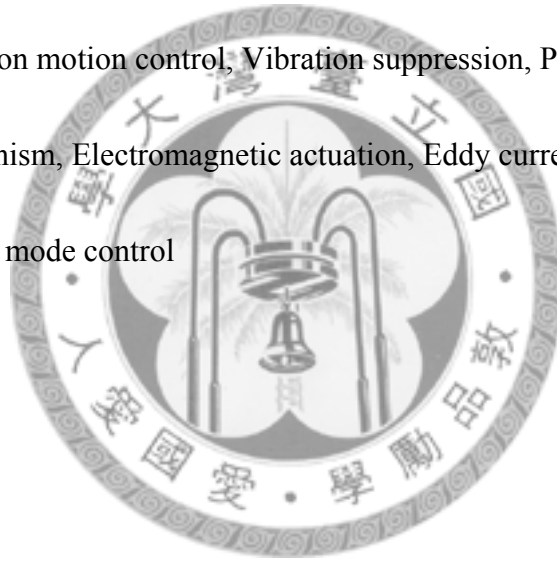
Table of Contents

List of Figures

List of Tables

Chapter 1
Introduction

1.1　Motivation and goal

The role of the multi-DOF (Degree-of-freedom) and high precision positioning stages becomes more and more important during the development of the micro- and nano-scale technology [1]. Positioning stages with high resolution, good repeatability and load capacity are essential to the applications of the most advanced researches. For the researches of Scanning Probe Microscope (SPM) or Atomic Force Microscope (AFM) [2][3], in order to create the three-dimensional surface topographic images of the specimens with resolutions of all dimensions down to the nanometer or Angstrom scales, the multi-DOF positioning stages providing capabilities of ultra-high resolution motions are necessary. For the modern fabrication, inspection and package processes, in which precision positioning and manipulation of the very small objects are purposed [4][5], and hence the multi-DOF precision positioning stages are also imperative.

In precision positioning, friction is the main obstacle, i.e., it is one of the most important factors limiting the performance in the precise positioning application.

Ball-screws drivers are popularly used in traditional positioning stages. Unfortunately, it will cause undesirable disturbances and backlash due to contact of bearing element. These unfavorable factors will be likely to affect our efforts to achieve high precision motion. Considerable effects to model and compensate the effect of friction have been made for years [6][7]. But there is no way more direct and effective than the avoidance of contact. Two modern non-contact approaches are usually utilized to avoid the effect of friction: the magnetic levitation and flexure hinge suspension.

In magnetic levitation (Maglev), the stage is levitated by the electromagnetic force. The Maglev technology has been widely used on transportation system, and it is also useful in precision positioning. Another modern approach uses the flexure mechanism for suspension and guidance of the positioning stage, and the principle is to fully utilize the elastic deformation of the very thin cantilever beams. Without contact, friction, stiction, and backlash are removed, and hence the flexure mechanism facilitates smooth and high resolution motion of the positioning stage. It is worthwhile to note that the actuation adapted in most researches involving positioning stage with flexure mechanism utilizes piezoelectric actuators. However, typical piezoelectric actuators can merely travel in a linear range of micrometers due to the hystersis property, which severely limits the traveling range of the positioning stage. Most piezoelectric actuators

can only handle small range motion and may not be suitable to achieve precision motion with large moving range.

In our previous researches [8][9], electromagnetic actuations are used. There are many advantages associated with electromagnetic actuating technology, such as no contamination, no friction, fast response, high acceleration, large travel range, low noise, and low cost. The flexure mechanism positioning stage with electromagnetic actuators thus has the potential to achieve high precision control and to achieve a longer traveling range typically ten or fifteen times of that from the same stage but using piezoelectric actuator.

The aiming target of this thesis is to develop a low-cost and compact positioning stage with large traveling range, which is suspended by flexure mechanism and driven by the electromagnetic actuators.

In the following section, the literature on the related work and the results of our previous researches will be introduced.

1.2   Literature Survey

1.2.1   Precision positioning utilizing flexure mechanism

The positioning stage proposed in this thesis work utilizes flexure mechanism based on the property of elastic deformation of the flexure material itself. A general discussion on designing flexure hinge mechanisms was given in detail by Smith [10]. The precision devices use flexure mechanism as replacement of conventional hinges, which in turn prevents the problems of friction and backlash. One degree-of-freedom (DOF) nanopositioning system (developed in Asylum Research, Santa Barbara, Univ. of California) has been proposed [11], as shown in Fig. 1-1. The work equipped with the symmetrical geometry to achieve nanometer resolution with x-axis or y-axis translation or even z-axis rotation has been reported [12], as shown in Fig. 1-2. Similarly, a planar three DOF parallel-type structure has also been designed in [13], as shown in Fig. 1-3.

Besides the mechanisms mentioned above, there are still considerable efforts devoted to the mechanism design to enhance the stiffness of the precision device, which together lead to more complicated [14], as shown in Fig. 1-4.
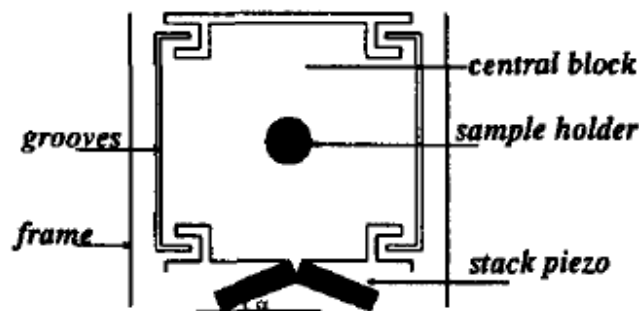
Fig. 1-1 The exploded view of the flexure and evaluation stages [11]
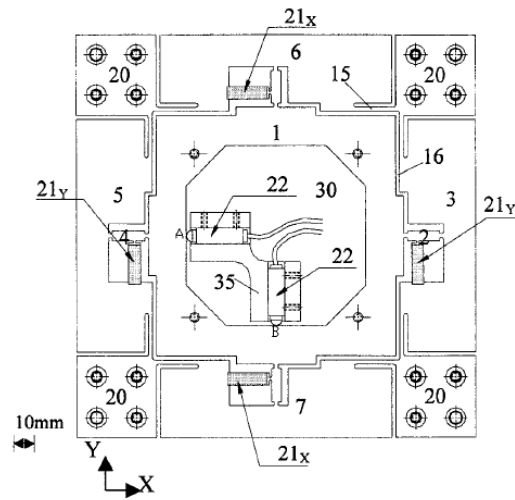
Fig. 1-2 Translation stage proposed by Chang [12]
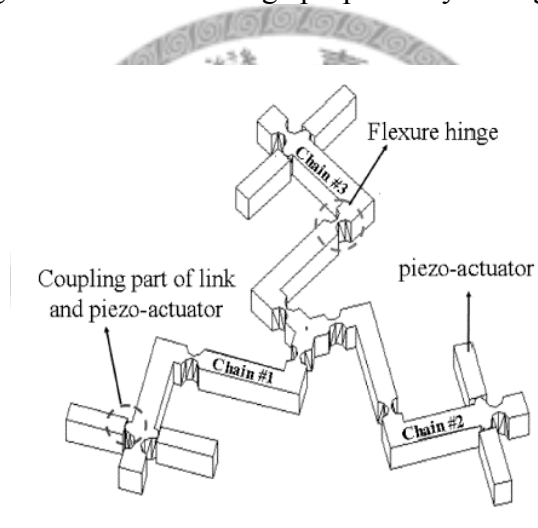
Fig. 1-3 Schematic of the 3-DOF microparallel mechanism [13]
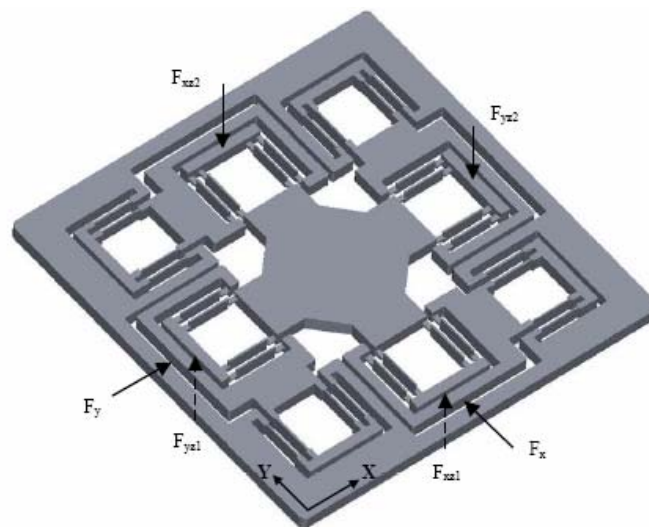
Fig. 1-4 The complex flexure mechanism with high stiffness [14]

Moreover, Li and Xu [15] proposed a 2-DOF compliant parallel manipulator as shown in Fig. 1-5. The workspace of the stage turns out to be rougnly 180 x180 μm. They optimized the kinematic design to enlarge the workspace by finite element analysis.
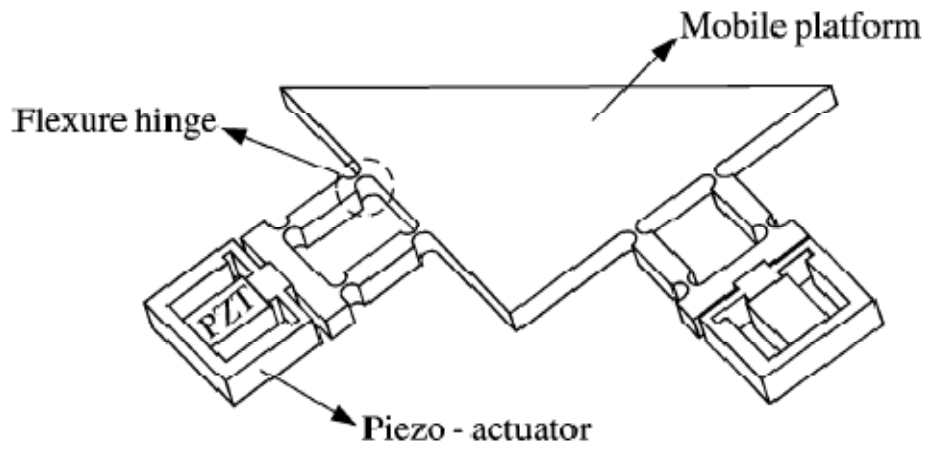
Fig. 1-5 The 2-DOF compliant parallel manipulator [15]

1.2.2 Our previous research

In the previous researches of our lab, precision positioning stages using flexure mechanism have been developed. Huang [8] first proposed a 3-DOF flexure mechanism and Wu [9] next proposed a 6-DOF flexure mechanism. The electromagnetic actuators were instead of the common piezoelectric ones used in these researches in order to extend the traveling range of the positioning stage. However, vibration of flexure mechanism becomes significantly severe under the circumstances without support of the rigid piezoelectric actuators. It is noteworthy that such vibration is a serious issue to

control the positioning stage.
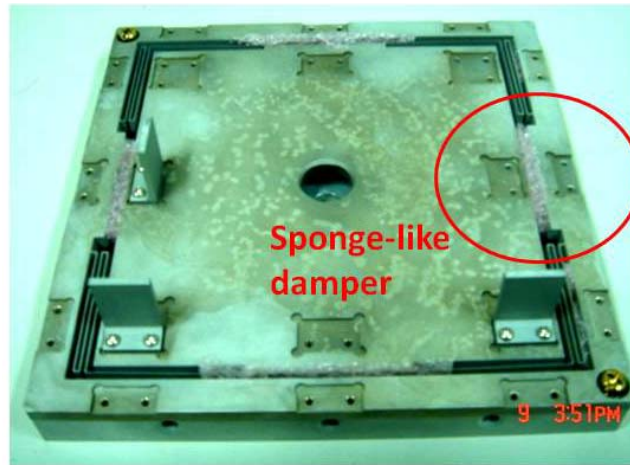
Fig. 1-6 The sponge-like damper used to suppress vibration

Therefore, sponge-like material was used to act as the mechanical damper to suppress the vibration, which is as shown in Fig. 1-6. But such damper is a contact device, and its use contradicts to the underlying designing principle of a noncontact and frictionless precision positioning stage. An important objective of this thesis is to seek an adequate contactless damper nether than a contact one to serve as vibration remover.

1.3   Contribution

In this thesis, a novel planar positioning stage including mechanism, control, and analysis are successfully presented. In particular, there are several main goals that have been achieved here: (1) to design a linear electromagnetic actuator and a built-in contactless electromagnetic damper to suppress the vibration of flexure mechanism, (2)

to integrate the electromagnetic devices and the parallel flexure mechanism for planar positioning system, (3) to derive a precise measurement methodology for the reliable and accurate measurements of the position and posture of positioning stage, (4) to develop an advanced adaptive sliding-mode controller, (5) to perform numerical simulation to validate the satisfactory performance, and (6) to perform extensive experiments to validate the excellent performance.

1.4   Thesis Organization

There are totally seven chapters in this thesis. It starts with an introductory chapter which motivates this research and introduces the state-of-the-art research results in precision positioning devices. In Chapter 2 , we review some basic theories of electromagnetism, properties of the permanent magnet, the analysis of the energy method, and the introduction on flexure mechanism. The following chapter, Chapter 3 , describes the design concept for fulfilling the desired motion behavior through description of the detailed specifications of various components in the novel 3-DOF positioning stage. Next, the force allocation, the sensing methodology, the mathematic model, the dynamic behavior and the system identification of the 3-DOF positioning stage will be analyzed and derived in Chapter 4 . Then, proper controller design, which based on adaptive sliding-mode control technique, and the numerical simulations are

conducted in 0. Subsequently in order to validate the effectiveness and appealing performance of the design, extensive experimental results are provided in Chapter 6 .

Finally, we make some conclusions to sum up the results in this thesis in Chapter 7 .

Chapter 2
Preliminary

2.1　Basic Theories of Electromagnetic

In this section, we will briefly review the basic theories of electromagnetic that will be used in our system design and analysis, specifically concerning Lorentz force principle and eddy current phenomenon.

2.1.1　Lorentz force principle

The Lorentz force equation is the basis for governing all magnetic forces. Magnetic fields are a description of the relativistic effects that occur among moving charges, which are a direct result of the Lorentz transformation of the Coulomb force.

The force dF on a current element Idl immersed in a magnetic field B is given as:

$$dF = I \times Bdl \qquad (2.1)$$

Note that Idl cannot exist by itself as it must be part of a complete loop or circuit. On such a loop, the total summed force is

$$F = \oint Idl \times B \tag{2.2}$$

As shown in Fig. 2-1, in order to simplify (2.2), a segment with length L of a long straight wire is assumed to be exposed to a uniform magnetic field B that is perpendicular to the wire, and the return path of the wire is to be outside the field. Then, this integral can be expressed as a scalar solution

$$F = ILB \tag{2.3}$$

where I is the current carried on the conduction wires, L is the length of the conduction wires through the magnetic field, and B is the external magnetic flux density. If there are N-turn wires through the magnetic field, then

$$F = NILB \tag{2.4}$$

It is important to note that the force on the conductor is given only by (2.4) if the field due to the current I can be neglected.
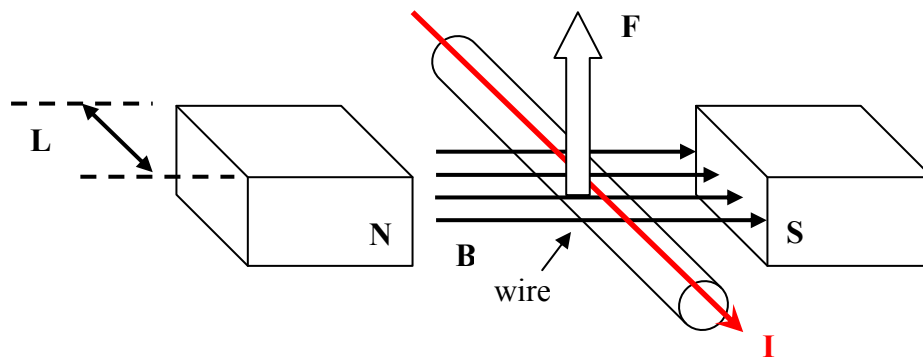
Fig. 2-1 Lorentz force principle

The electromagnetic actuator designed based on Lorentz force principle are often applied when high bandwidth dynamic are to be achieved. Examples are voice coil actuators, loudspeakers, synchronous brushless DC motors, and so on.

2.1.2 Eddy current phenomenon

When a non-ferromagnetic conductor moves in a magnetic field, or a moving and varying magnetic field intersects a non-ferromagnetic conductor, the relative motion causes a circulating current within the conductor. Figure 2-2 shows that when a conductor is moving in the magnetic field B with the velocity v, the eddy current i is generated within the conductor. The interaction between the current and the magnetic field will generate a force to resist the relative motion between the magnetic field and the conductor. Because of the resistance of the conductor, the eddy current will dissipate and energy of the system will be transformed into heat.

13
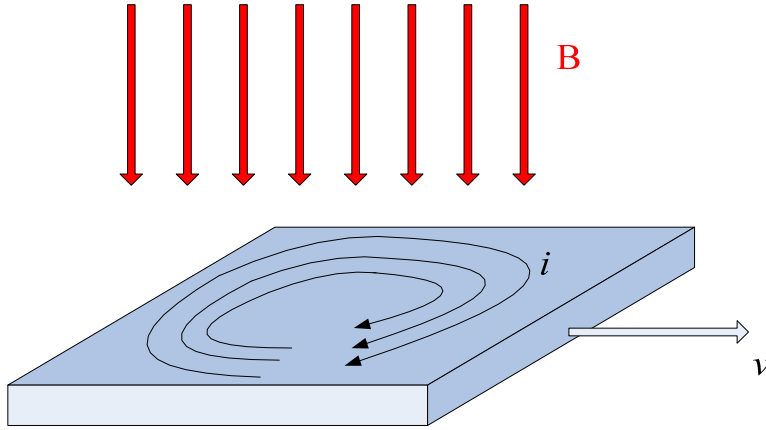
Fig. 2-2 The eddy current phenomenon

For the researches on, say, electric motors, the eddy current phenomenon will reduce the efficiency and should be avoided. However, it can be used to remove the excessive energy from the system to physical contact. There are lots of practical applications of eddy current devices [18], including electromagnetic braking, magnetic damping, and passive vibration control.

Bae et *al.* [19] proposed the design and modeling of a passive eddy current damper shown in Fig. 2-3. The eddy current damper (ECD) consists of a copper plate and a pair of magnets. The experimental results show that the vibration of the cantilever beam has successfully been suppressed by the additional ECD. The magnitude of the damping force is also described in [19] as:

$$F_d = -\sigma \delta v B^2 S \alpha \qquad (2.5)$$

where σ is the thickness of the conductor in the magnetic field, δ is the conductivity, v

is the velocity, B is the magnetic flux density, S is the effective area, and α is the dimension parameter.
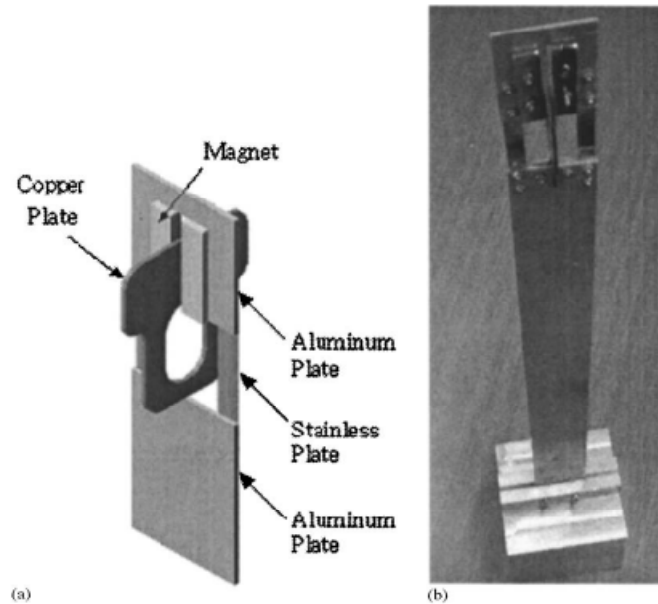
Fig. 2-3 Eddy current damper to suppress vibration [19]

2.2　Properties of Permanent Magnet

Since we use the electromagnetic actuators, the magnet characteristics cannot be neglected. In this section, we will review briefly some basic properties of permanent magnet (PM), and then present the detailed data of the used magnets, such as maximum energy product, coercive force, and temperature coefficient, etc.

According to Gauss Law, the magnetic flux continuity law can be described as follows:

$$\nabla \cdot \mu_0 \vec{H} = -\nabla \cdot \mu_0 \vec{M} \tag{2.6}$$

When a magnetic field $\vec{H}$ is applied to a ferromagnetic substance, the material

will be magnetized with the internal flux density $\vec{B}$ given by

$$\vec{M} = N\vec{m} \tag{2.7}$$

$$\vec{B} = \mu_0 \left(\vec{H} + \vec{M} \right) \tag{2.8}$$

where $\vec{M}$ is the induced magnetization density, defined as the magnetic dipole

moment per unit volume, and N is the number of dipoles per unit volume. By (2.7) and

(2.8), we can obtain the *B-H* curve by varying the field $\vec{H}$ and measuring the flux

density $\vec{B}$. Figure 2-4 is a typical *B-H* curve of a ferromagnetic material.
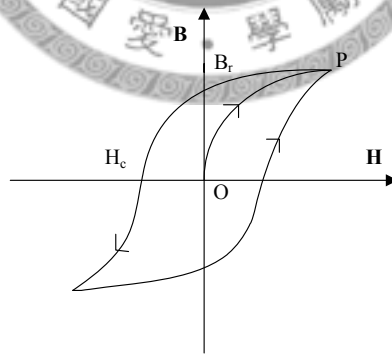
Fig. 2-4 *B-H* curve of a typical ferromagnetic material

From Fig. 2-4, the curve OP is the initial magnetizing curve, and point P is the

saturation point that means the material reaches its maximum magnetization. Once we

vary $\vec{H}$ from positive value to negative value and then back to positive value again,

16

the *B-H* curve forms a loop called hysteresis. The intersection of the loop and the $\vec{B}$

axis is known as the remanence, residual magnetization, or residual flux density,

denoted as $\vec{B_r}$, which is the magnetic flux density inside the magnet when the external

field $\vec{H}$ is reduced to zero. Moreover, $\vec{H_c}$ is known as the coercivity or coercive

force which is the external field needed to completely demagnetize the substance.

By (2.6), when external $\vec{H}$ is removed, the residual flux density inside the

ferromagnetic material is

$$\vec{B_r} = \vec{M} \tag{2.9}$$

which indicates that the material has become a PM with residual flux density $\vec{M}$.

Then, the magnetization of this PM can be expressed as:

$$\vec{M} = \vec{B_r} \tag{2.10}$$

Therefore, the dipole moment resulting from the definition of magnetization is then

given as:

$$\vec{m} = \vec{B_r}V \tag{2.11}$$

where *V* is the volume of this PM.

In the following, comparisons among different magnets with their specific properties shown in Table 2-1 will be given. Among the listed magnet materials, Ferrite, also known as ceramic magnet, provides the lowest maximum energy product BH_{max} and the lowest residual induction $\vec{B}_r$. Ceramic materials are hard and brittle and are extensively used in consumer products, and on the back of popular refrigerator magnets.

Rare-earth elements are the most popular materials used to produce the strong magnets. One of the strong magnets is Samarium Cobalt, which has high $\vec{B}_r$, high $\vec{H}_c$, relatively high maximum energy product (BH_{max}), and also higher cost than NdFeB. Commonly, its energy product ranges from $18\,MGOe$ (Mega Gauss Oersteds) to about $32\,MGOe$. The most familiar one of the strong magnets is NdFeB or, for more accurately, sintered NdFeB magnet, whose property is similar to that of SmCo but which belongs to the most powerful class and is commercially available today. Its energy product ranges from $2.8\,MGOe$ to about $48\,MGOe$. Therefore, NdFeB magnet is the most reliable choice to provide high magnetic force in our system.

Table 2-1 Characteristics of Magnet

Property	Unit	AlNiCo	Ferrite		Rare Earth			
		AlNiCo Magnet	Sintered Ferrite Magnet	Bonded Ferrite Magnet	Sintered SmCo Magnet	Bonded SmCo Magnet	Sintered NdFeB Magnet	Bonded NdFeB Magnet
Residual Induction (Br)	kG	11.5	4.4	3.1	11.6	8.5	14.2	7.3
Coercive Force (bHc)	kOe	1.6	2.8	2.4	10.1	7.6	11.7	5.7
Intrinsic Coercivity (iHc)	kOe							
Maximum Energy Product (BH)max	MGOe	11	4.6	2.2	32	17	48	11
Temperature Coefficient α (Br)	%/K	-0.02	-0.18		-0.0.3	-0.03	-0.11	-0.10
Temperature Coefficient β (iHc)	%/K	~0	+0.4		-0.2	-0.2	-0.6	-0.4
Curie Temperature Tc	℃	845	460		795	795	335	335
Flexure Strength	kgf/mm^2	28	13		12		25	
Density ρ	g/cm^3	7.3	5.0		8.4	7.0	7.5	6.0
Hardness Hv		650	530		550	80-120	600	80-120
Electrical Resistivity	$\mu\Omega\cdot$cm	60	>1010		80	44000	150	26000

(Data from Spin Technology Corp. in Taiwan.)

We can conclude that NdFeB material is the best choice at present, since AlNiCo

has low coercivity, Ferrite has low remanence, and Samarium Cobalt magnets are still

expensive. Table 2-2 indicates several characteristics of the NdFeB magnets.

Table 2-2 Specifications of NdFeB

Specifications	NdFeB
Remanence (T)	1.29
Coercivity (kA/m)	990
Maximum energy product (kJ/m^3)	320
Density (g/cm^3)	7.49
Curie temperature (^0C)	310
Resistivity ($\mu\Omega\text{m}$)	6

2.3   Basic Theories of Energy Methods

In this section, we will introduce how to apply energy method to solve problems

involving deflection. Then, Castigliano's theorem is an important theory to be referred

to, which is used here to determine the stiffness of the flexure mechanism. For more

details, readers are suggested to refer to the work [17].

2.3.1   External work and strain energy

First, we will define the work caused by an external force and a couple moment.

Work of a force

In mechanics, a force does work when it undergoes a displacement dx that is in the direction the same as that of the force. The work done is a scalar, defined as $dU_e = Fdx$. If the total displacement is x, the work becomes

$$U_e = \int_0^x Fdx$$ (2.12)

Work of a couple moment

A couple moment **M** does work when it undergoes a rotational displacement $d\theta$ along its direction of action. The work done is defined as $dU_e = Md\theta$. If the total angle of rotational displacement is θ rad., the work becomes

$$U_e = \int_0^\theta Md\theta$$ (2.13)

When loads are applied to a body, they will deform the material. Provided no energy is lost in the form of heat, the external work done by the loads will be converted into internal work called **strain energy**. This energy, which is always positive, is stored in the body and is caused by the action of either normal or shear stress.

Normal Stress

In general, if the body is subjected only to a uni-axial normal stress σ, acting in a

21

specified direction, the strain energy in the body is

$$U_i = \int_V \frac{\sigma \varepsilon}{2} dV \qquad (2.14)$$

Also, if the material behaves in a linear-elastic manner, Hooke's law suggests $\sigma = E\varepsilon$, whereby we can express the strain energy in terms of the normal stress as

$$U_i = \int_V \frac{\sigma^2}{2E} dV \qquad (2.15)$$

where E is the Young's module.

2.3.2 Strain energy for bending moment

Since a bending moment applied to a straight prismatic member develops normal stress in the member, we can use (2.15) to determine the strain energy stored in the member due to bending. Considering a bending applied to the axis-symmetric beam as shown in Fig. 2-5, the internal moment here is M, and hence the normal stress acting on the arbitrary element at a distance y from the neutral axis is $\sigma = My/I$. If the volume of the element is $dV = dAdx$, where dA is the area of its exposed face and dx is its length, the elastic strain energy in the beam is

$$U_i = \int_V \frac{\sigma^2}{2E} dV = \int_V \frac{1}{2E} (\frac{My}{I})^2 dAdx \qquad (2.16)$$

22

The integral over the volume can be expressed as the product of an integral over the beam's cross-sectional area A and an integral over its length L. Thus,

$$U_i = \left[\int_0^L \frac{M^2}{2EI^2} dx \right] \left[\int_A y^2 dA \right] \tag{2.17}$$

Realizing that the area integral represents the moment of inertia I of the beam about the neutral axis, the final result can be re-expressed as:

$$U_i = \int_0^L \frac{M^2}{2EI} dx \tag{2.18}$$
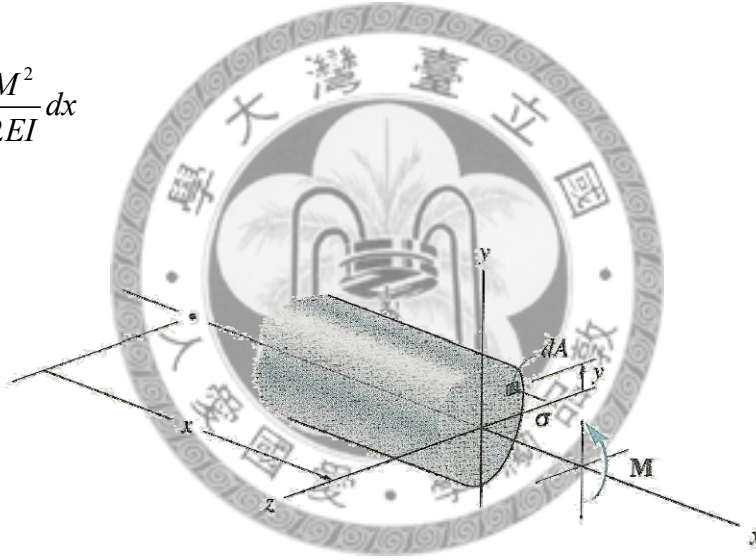
Fig. 2-5 Axis-symmetric beam

2.3.3 Castigiano's theorem

The internal strain energy for a beam is caused by both bending and shear. However, if the beam is long and slender, the strain energy due to shear can be neglected compared with that of bending. Assuming this to be the case, the internal strain energy for a beam is given by (2.18). Substituting it into $\delta = \partial U / \partial P$, we can get:

$$\delta = \frac{\partial}{\partial P} \int_0^L \frac{M^2}{2EI} dx = \int_0^L M(\frac{\partial M}{\partial P}) \frac{dx}{EI} \qquad (2.19)$$

Where the variables used are defined below:

$\delta =$ displacement of the point caused by the real loads acting on the beam,

$P =$ external force of variable magnitude applied to the beam in the direction of δ,

$M =$ internal moment in the beam, expressed as a function of x and is caused by both the

force P and the loads on the beam,

$E =$ modulus of elasticity of the material,

$I =$ moment of inertia of cross-sectional area computed about the neutral axis.

If the slope at a point on the elastic curve is to be determined the partial derivative

of the internal moment M with respect to the external couple moment M' acting at the

point must be found. For this case,

$$\theta = \int_0^L M(\frac{\partial M}{\partial M'}) \frac{dx}{EI} \qquad (2.20)$$

2.4 Flexure Mechanism

The most important advantage of flexure mechanism is frictionless and stictionless

which relies on the elastic deformation of material. Sliding and rolling effects are

completely eliminated in the devices using flexure mechanism. Flexures have been used

(1) as bearings to provide smooth and guided motion, when in precision motion stages;

(2) as springs to provide preload, when in the brushes of a DC motor or a camera lens cap; (3) to avoid over-constraint, as in the case of bellows or helical coupling; (4) as clamping devices, for example, the collets of a lathe; (5) for elastic averaging as in a windshield wiper; and (6) for energy storage such as, in a bow or a catapult. Above all, it encompasses applications with regard to the transmission of force, displacement as well as energy.

In our work, flexure mechanism is used as the suspension of precision positioning stages. The motion is generated due to molecular level deformation, which results in two primary characteristics of flexures – smooth motion and small range of motion, and the phenomena of friction, stiction and backlash are completely eliminated. On the other hand, flexure mechanisms allow for very clean and precise motion.
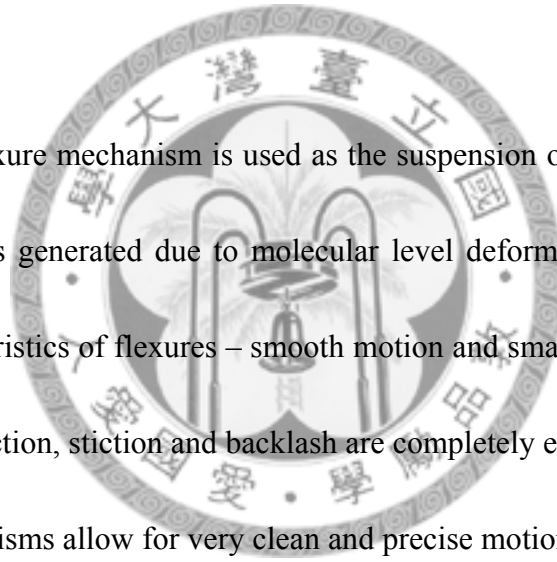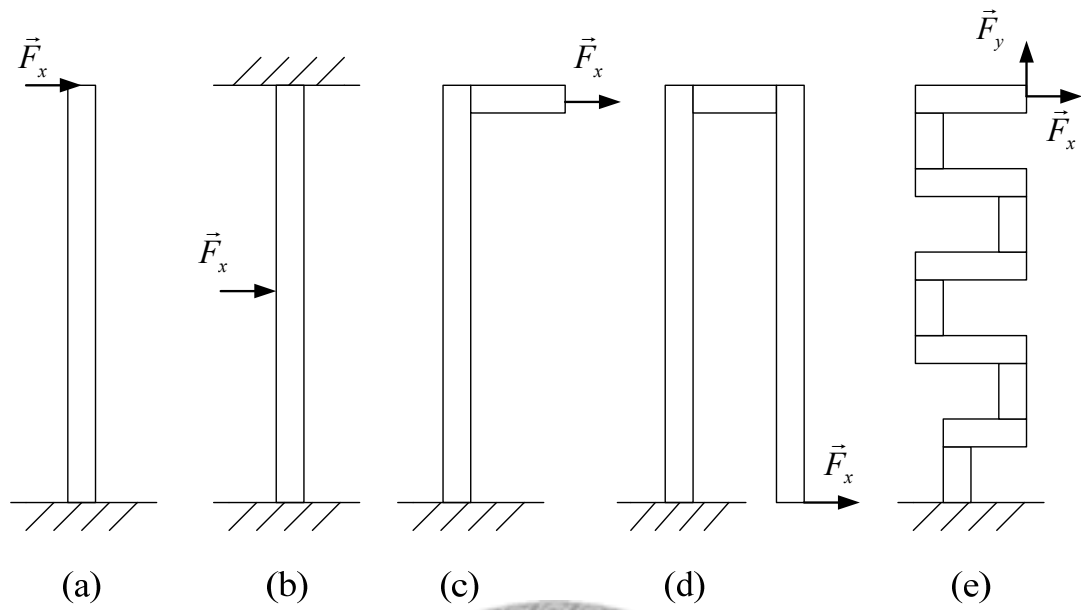
Fig. 2-6 Common flexure types: (a) simple cantilever, (b) clamped-clamped,
(c) crab-leg, (d) folded-flexure, (e) serpentine

There are several kinds of flexure type such as simple cantilever beam, clamped-clamped flexure, crab-leg flexure, folded flexure, and serpentine flexure as shown in Fig. 2-6. These kinds of flexures generate one DOF motion along the direction of force. In the following, we will give some analyses of characteristics of these flexure mechanisms.

Consider the simple cantilever beam in Fig. 2-7 with a rectangular cross section, and let it be subjected to a load P at its end. Now, we want to determine the displacement of the load.
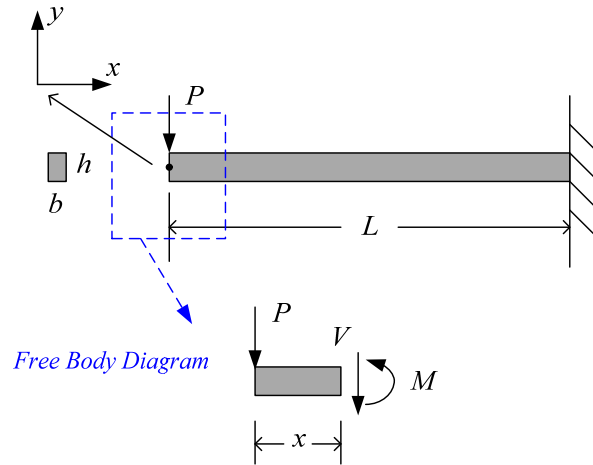
Fig. 2-7 Cantilevered beam and its free body diagram

It is assumed that we have known the material characteristics, and EI is constant. Here, E means the Young's modulus, and I means the inertia mass. Then, clearly, a small deflection on the elastic beam will result in

$$\frac{d^2 y}{dx^2} = \frac{M(x)}{EI} \tag{2.21}$$

According to free body diagram, we can get

$$\sum Force = 0 \implies V = -P \tag{2.22}$$

$$\sum Moment = 0 \implies M = -Px \tag{2.23}$$

Using (2.21) ~ (2.23), and applying the boundary conditions, we can obtain the deflection curve as

$$y = \frac{P}{6EI}(-x^3 + 3L^2 x - 2L^3) \tag{2.24}$$

27

so that the tip deflection can be easily derived as $y\big|_{x=0} = \dfrac{-P}{3EI}L^3 \triangleq \dfrac{F}{-k}$. As a result, the

spring constant k can be obtained as

$$k = \frac{3EI}{L^3} \qquad\qquad (2.25)$$

After discussing the simplest cantilevered beam, now we will discuss the

quad-symmetric clamped-clamped flexure mechanism. Due to its symmetric structure,

this mechanism only generates one DOF motion. As shown in Fig. 2-8, we can model

the structure as four guided-end beams.
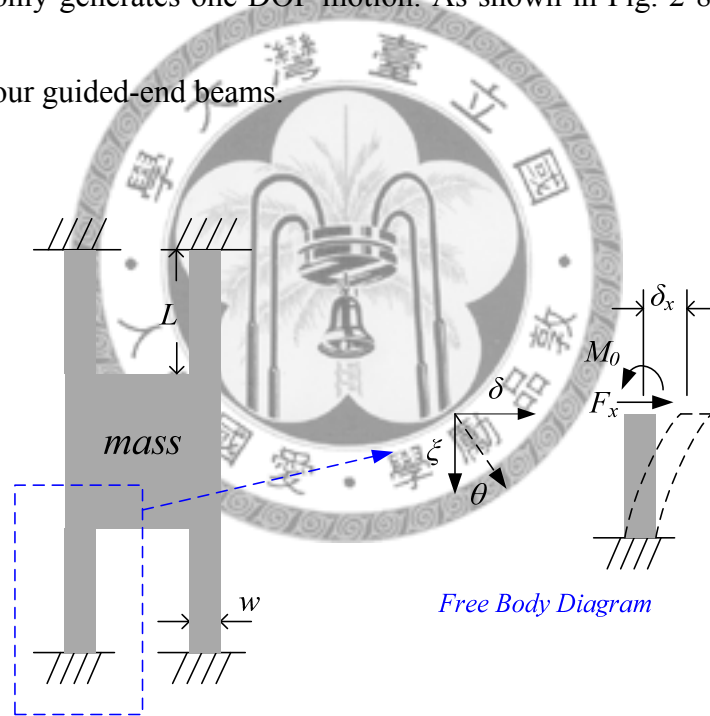
Fig. 2-8 Quad-symmetric clamped-clamped flexure and its free body diagram

According to the free body diagram, an external force F_x and a bending moment

M_0 can be applied to a body to find the displacement δ_x and the corresponding spring

constant k_x. Therefore, the bending moment of the beam is found to be

$$M = M_0 - F_x \xi \tag{2.26}$$

By (2.18), the associated strain energy of the beam is

$$U = \int_0^L \frac{M^2}{2EI} d\xi \tag{2.27}$$

Now, rewrite the *Castigliano's Theorem*, mentioned in (2.19) and (2.20), as follows:

$$U = \int_0^L \frac{M(x)^2}{2EI} dx \ , \ \delta = \frac{\partial U}{\partial F_\delta} \ , \ \theta_0 = \frac{\partial U}{\partial M_0} \tag{2.28}$$

which together with the constraint $\theta_0 = 0$ and (2.26), will lead to the following

relation:

$$\begin{aligned}
\theta_0 &= \frac{\partial U}{\partial M_0} = \int_0^L \frac{M}{EI} \frac{\partial M}{\partial M_0} d\xi \\
&= \frac{1}{EI} \int_0^L (M_0 - F_x \xi) d\xi = 0
\end{aligned} \tag{2.29}$$

Now, substituting $M_0 = \frac{F_x L}{2}$ into the (2.26), we can then obtain

$$M = F_x (\frac{L}{2} - \xi) \tag{2.30}$$

Again, through use of *Castigliano's Theorem*, (2.28), and its substitution into

(2.30), we finally derive the displacement as:

$$\delta_x = \frac{\partial U}{\partial F_x}$$

$$= \int_0^L \frac{M}{EI} \frac{\partial M}{\partial F_x} d\xi$$

$$= \int_0^L \frac{F_x(\frac{L}{2} - \xi)}{EI} (\frac{L}{2} - \xi) d\xi \qquad (2.31)$$

$$= \frac{F_x}{EI} \int_0^L (\frac{L}{2} - \xi)^2 d\xi = \frac{F_x L^3}{12EI}$$

As a consequence, the spring constant of the beam and of the quad-symmetric

clamped-clamped flexure can readily be obtained as:

$$k_{x,beam} = \frac{F_x}{\delta_x} = \frac{12EI}{L^3}$$

$$k_x = 4 \cdot k_{x,beam} = \frac{48EI}{L^3} \qquad (2.32)$$

Besides the above two kinds, we will analyze another type of flexure, called

quad-symmetric crab-leg flexure mechanism, as shown in Fig. 2-9. The same as the

clamped-clamped flexure, this mechanism also only generates one DOF motion. It can

be modeled as four crab-leg flexure, and we divide every crab-leg into two parts, thigh

(beam a) and shin (beam b).
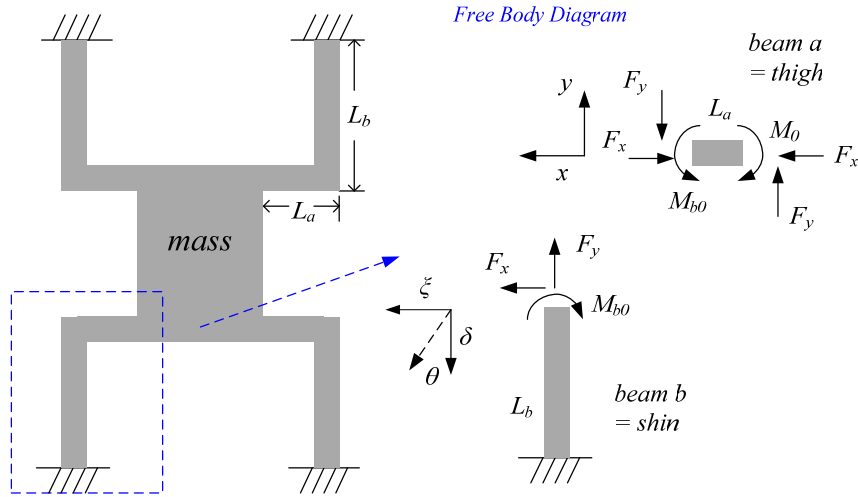
Fig. 2-9 Quad-symmetric crab-leg flexure and its free body diagram

For the purpose of analysis, likewise we apply F_x, F_y, and M_0 at the end of the thigh. According to the free body diagram, the bending moments of the thigh (M_a) and shin (M_b) can be respectively expressed as:

$$M_a = M_0 - F_y x \tag{2.33}$$

$$M_b = M_{b0} - F_x \xi = (M_0 - F_y L_a) - F_x \xi \tag{2.34}$$

We now use *Castigliano's Theorem*, (2.28), and apply the boundary conditions ($\theta_0 = 0$, $\delta_y = 0$) to find M_0 and F_y as:

$$\theta_0 = \frac{\partial U}{\partial M_0}$$

$$= \int_0^{L_a} \frac{M_a}{EI} \frac{\partial M_a}{\partial M_0} dx + \int_0^{L_b} \frac{M_b}{EI} \frac{\partial M_b}{\partial M_0} d\xi$$

$$= \frac{1}{EI} \left[\int_0^{L_a} (M_0 - F_y x) dx + \int_0^{L_b} (M_0 - F_y L_a - F_x \xi) d\xi \right] \qquad (2.35)$$

$$= \frac{1}{EI} \left[M_0(L_a + L_b) - \frac{F_y L_a^2}{2} - F_y L_a L_b - \frac{F_x L_b^2}{2} \right] = 0$$

so that

$$M_0 = \frac{L_b^2 F_x + 2 L_a L_b F_y + L_a^2 F_y}{2(L_a + L_b)} \qquad (2.36)$$

and

$$\delta_y = \frac{\partial U}{\partial F_y}$$

$$= \int_0^{L_a} \frac{M_a}{EI} \frac{\partial M_a}{\partial F_y} dx + \int_0^{L_b} \frac{M_b}{EI} \frac{\partial M_b}{\partial F_y} d\xi$$

$$= \frac{1}{EI} \left[\int_0^{L_a} (M_0 - F_y x)(-x) dx + \int_0^{L_b} (M_0 - F_y L_a - F_x \xi)(-L_a) d\xi \right] \qquad (2.37)$$

$$= \frac{1}{EI} \left[-\frac{M_0 L_a^2}{2} + \frac{F_y L_a^3}{3} - M_0 L_a L_b + F_y L_a^2 L_b - \frac{F_x L_a L_b^2}{2} \right] = 0$$

so that

$$F_y = \frac{3 L_b^2 F_x}{L_a(L_a + 4 L_b)} \qquad (2.38)$$

Note that M_0 and F_y are both functions of F_x.

Now, we use *Castigliano's Theorem* again to derive δ_x as:

32

$$\delta_x = \frac{\partial U}{\partial F_x}$$

$$= \int_0^{L_a} \frac{M_a}{EI} \frac{\partial M_a}{\partial F_x} dx + \int_0^{L_b} \frac{M_b}{EI} \frac{\partial M_b}{\partial F_x} d\xi$$

$$= \frac{1}{EI} \left[\int_0^{L_b} (M_0 - F_y L_a - F_x \xi)(-\xi) d\xi \right]$$

$$= \frac{1}{EI} \left[-\frac{M_0 L_b^2}{2} - F_y L_a L_b + \frac{F_x L_b^2}{2} \right] \tag{2.39}$$

After substituting (2.36) and (2.38) into (2.39), we readily have

$$\delta_x = \frac{1}{EI} \left[-\frac{M_0 L_b^2}{2} - F_y L_a L_b + \frac{F_x L_b^2}{2} \right]$$

$$= \frac{1}{EI} \left[-\frac{L_b^2 F_x + 2 L_a L_b F_y + L_a^2 F_y L_a^2}{2(L_a + L_b)} - \frac{3 L_b^2 F_x}{L_a (L_a + 4 L_b)} L_a L_b + \frac{F_x L_b^2}{2} \right] \tag{2.40}$$

$$= \frac{L_b^3 (L_a + L_b) F_x}{3 EI (L_a + 4 L_b)},$$

from which the spring constant of the quad-symmetric crab-leg flexure can be readily

derived as:

$$k_x = \frac{F_x}{\delta_x} = \frac{3 EI (L_a + 4 L_b)}{L_b^3 (L_a + L_b)} \tag{2.41}$$

2.5   Measurement Error

There is no perfect measurement system in the real world. The error comes from

imperfect sensor assembly and alignment, measurement methodology, and signal noise.

This section would discuss two common errors, namely, Abbe error and cosine error.

The compensation of the two errors will be described in the following section so that an

accurate and reliable measurement methodology can be properly derived.

2.5.1 Abbe principle and Abbe error

When the axis to be measured and the axis of measurement are not coaxial, a measurement error will occur due to the offset between two axes. In late 1800s, Dr. Ernest Abbe investigated the issue and proposed this principle: the measuring system should be placed coaxially with the axis which is to be measured. Figure 2-10 shows the Abbe error, which can be estimated as:

$$e_{Abbe} = D \tan \theta \qquad (2.42)$$

where D is the offset between the two axes.
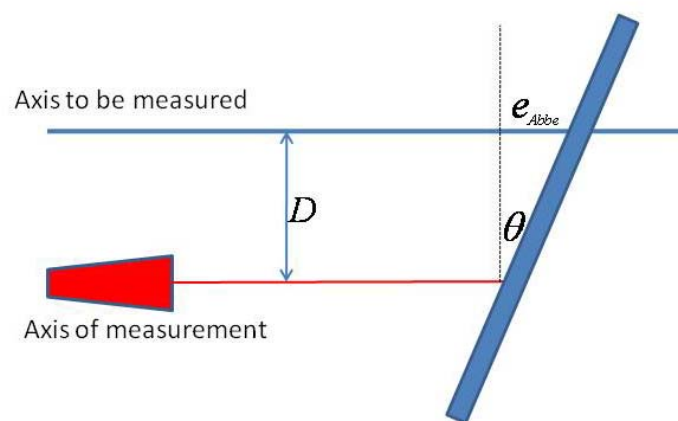
Fig. 2-10 Abbe error

2.5.2 Cosine error

Cosine error occurs when the axis of measurement and axis which is to measured are not completely parallel. In Fig. 2-11, the included angel θ causes that the measured displacement *x'* is different from the real displacement *x*. The cosine error hence results from inadequate alignment between the motion stage and the sensor.
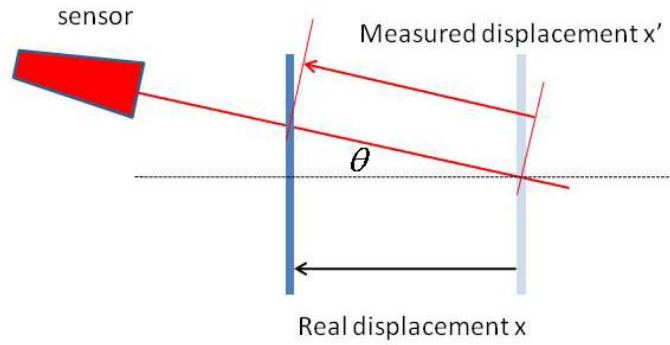
Fig. 2-11 Cosine error

From the above figure, the relationship between the measured displacement *x'* and the real displacement *x* can be expressed as:

$$x' = \frac{1}{\sin\theta} x \qquad\qquad (2.43)$$

Then, the cosine error can be estimated as:

$$e_{\cos} = x' - x = \frac{1}{\sin\theta} x - x = x(\sec\theta - 1) \qquad\qquad (2.44)$$

Chapter 3
Mechatronic Design

The aiming target of our research is a positioning stage with high positioning accuracy, large moving range with multiple DOFs. To realize these properties, we adopt the planar parallel flexure mechanism as the suspension of the moving stage due to its frictionless effect, electromagnetic actuator for its low cost, and appropriate arrangement of measurement system in order to precisely measure the 3 DOF displacements of the three degrees of freedom of the designed system.

The related researches and needed background knowledge have been reviewed and introduced in the previous chapter. In this chapter, the design concept of the proposed positioning stage will be introduced, including the flexure suspension mechanism, electromagnetic actuator and damper, measuring system, and the integration of all the components.

3.1   Design Strategies

Now, we list all the design objectives that we want to accomplish as follows:

1. high positioning accuracy,

2. long planar stroke,

3. fast positioning,

4. compact system.

The following subsections will translate these goals into actuator level requirements. Since most objectives are strongly coupled, we are not able to consider respective design separately.

3.1.1 High positioning accuracy

To attain high positioning accuracy, either the system needs a high disturbance rejection, or the external noise sources need to be shielded off. Moreover, the bits-resolution of AD/DA cards and the resolution of sensor are also some major factors to be concerned. Therefore, instead of investing on installation of expensive equipments, we set our design goal on how to utilize commonly available sensors and AD/DA cards on how to optimize the integrated performance up to respective performance limits of individual components.

To reject the large disturbance and obtain a high bandwidth, performance of the actively controlled system is usually limited by the controllability, linearity, and response time of the actuator and controller.

3.1.2   Long planar stroke

A larger positioning range within the same outer dimensions is advantageous. Normally, to reduce costs of production, parallel or batch processing is often applied to increase throughput of samples or products. Consequently, those larger specimens require larger strokes without the decreasing in speed and acceleration.

In the target application, the traveling range in using piezoelectric actuators is just 100 μm [13] due to the constraint of piezoelectric material's characteristics. In our system, because of fewer physical constraints, we choose electromagnetic actuator to enlarge the traveling range up to several mm.

3.1.3   Fast positioning

For the same reason mentioned in previous section, to increase the throughput of production, motion of any positioning system should be fast as possible so that it can become commercially attractive. For the transient response specification, the rise time and the settling time must be short. To fulfill such objective, we must have both a strong and high speed actuator and a well-designed mechanism which have a higher bandwidth.

3.1.4 Compact system

The positioning system is usually a part of a larger system, which leads to restrictions on the space available for the motor and bearings. These restrictions are even more severe under the circumstance of an expensive ultra clean or vacuum environment. Generally, the outer diameter of a positioning system will be less when there are more moving parts. The implication of the above is that the total positioning should be as compact as possible.

3.2 Electromagnetic Actuation and Damper

This section discusses the design of electromagnetic actuator and damper which will be utilized in this proposed positioning system. Generally, using a rotary motor to generate the linear reciprocating motion must incorporate the use of the transmission mechanism, such as ball-screws, gears, racks, etc., to change the rotating motion into the linear motion. However, the transmission mechanisms usually have problems of backlash and friction which severely influence the precision of positioning. Therefore, it is better to use electromagnetic actuator, so-called voice coil motor (VCM), due to its frictionless contact and non-backlash nature.

VCM is one kind of linear direct-current motor and is composed of permanent

magnets (PMs) and coils which are assembled appropriately. It can produce the linear thrust proportional to the current which flows through the magnetic field.
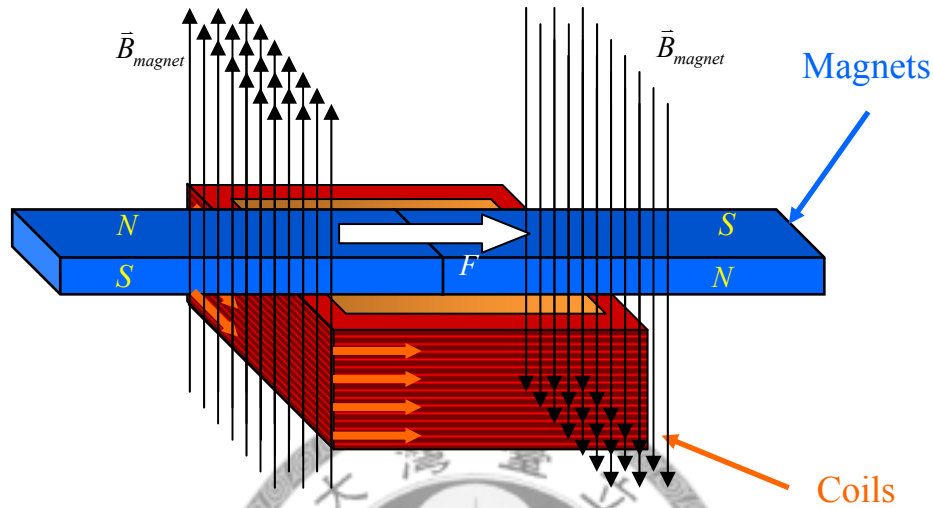
Fig. 3-1 The VCM actuator of our previous research [8]

Figure 3-1 shows the VCM actuator which is used in our previous research [8]. Two magnets are placed side by side with opposite polarity. The current-carrying coil would generate the force as shown in the above figure. But the assumption on the magnetic field produced by the magnets is not realistic. The real distribution of the magnetic field is highly non-uniform, so that the actuator suffers from the nonlinearity and the current/force relationship of the actuator will vary with the relative position between the magnets and the coils. This nonlinearity also limits the stroke of the actuator. In this section, we will discuss the design of a stronger linear electromagnetic actuator and the built-in electromagnetic damper.

3.2.1 Near-Uniform Magnetic Field

Since the nonlinearity of the electromagnetic actuator comes from the non-uniform magnetic field, intuitively a construction of uniform magnetic field will solve the issue. Figures 3-2 and 3-3 show the concept of constructing a near-uniform field. Two plate permanent magnets are installed inside a steel structure. A near-uniform magnetic field will be generated between the two plate permanent magnets and the outer magnetic flux will be confined within the ferromagnetic steel structure to form a closed loop flux path, as shown in Fig. 3-3. The dimension of the plate magnet is 60mm x 60mm x 2mm and its material is neodymium-iron-boron (NdFeB), the powerful rare earth permanent magnet material.
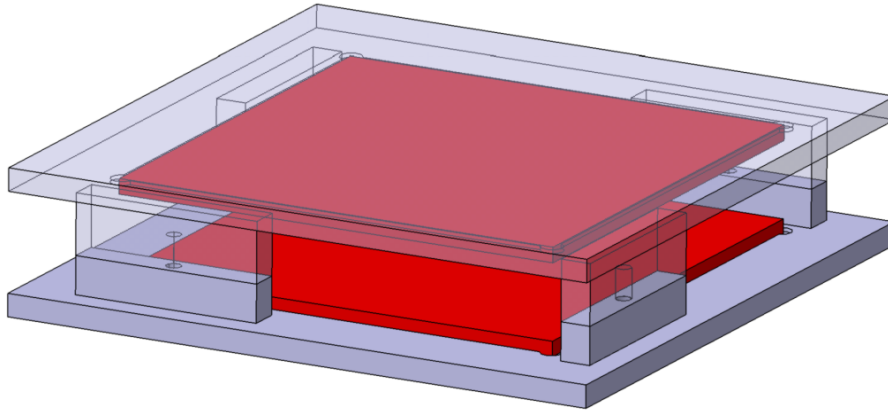
Fig. 3-2 The steel structure and permanent magnets
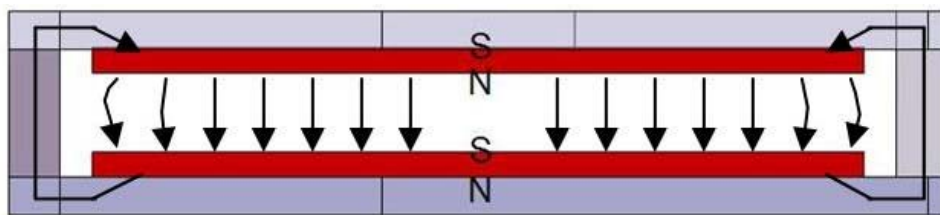
Fig. 3-3 The near-uniform magnetic field

To verify the near-uniform property of the constructed magnetic field, a finite element analysis is conducted as shown in Fig. 3-4. The outcome of such analysis does validate our viewpoint and the design.
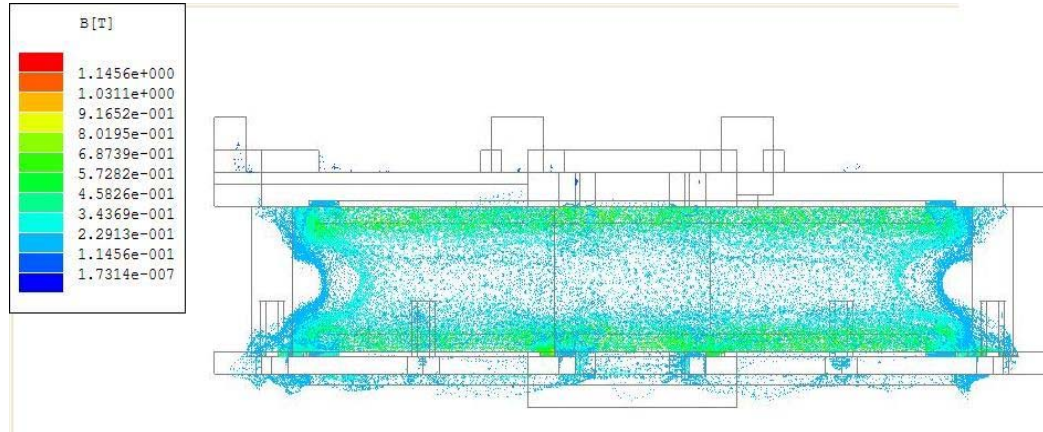
Fig. 3-4 The numerical simulation of magnetic field

3.2.2 The proposed electromagnetic actuator

Figures 3-5 and 3-6 show the configuration and assembly of the proposed electromagnetic actuators. A copper mounting is manufactured with the shape shown in Fig. 3-5 and is placed in the middle between the upper part and the lower part of the steel structure. Note that the two parts of the steel structure are attracted to each other by magnetic force and are connected through four rectangular holes opened on the copper mounting. The clearance between the steel structure and copper mounting is designed for the motion of the moving stage and is sufficient for the needed traveling range. Four square coils are placed on the copper mounting. When current is fed into the coils, the

interaction between the current and the intersected near-uniform magnetic field would

generate the electromagnetic force according to Lorentz force principle.
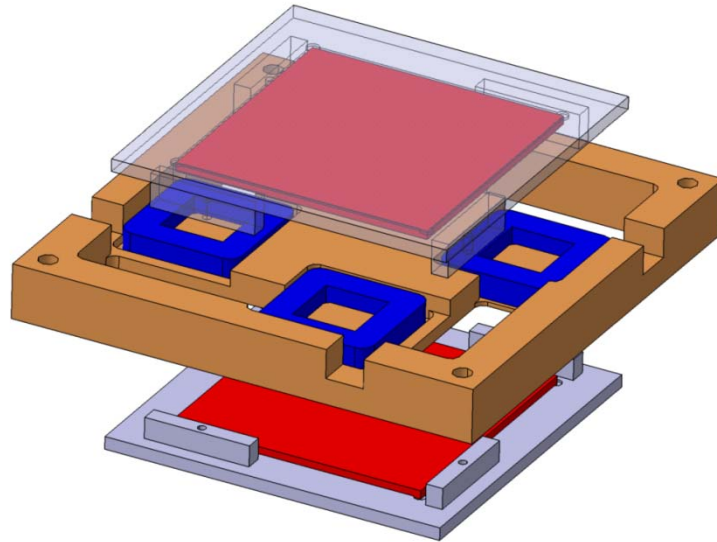
Fig. 3-5 The assembly of the VCM actuator
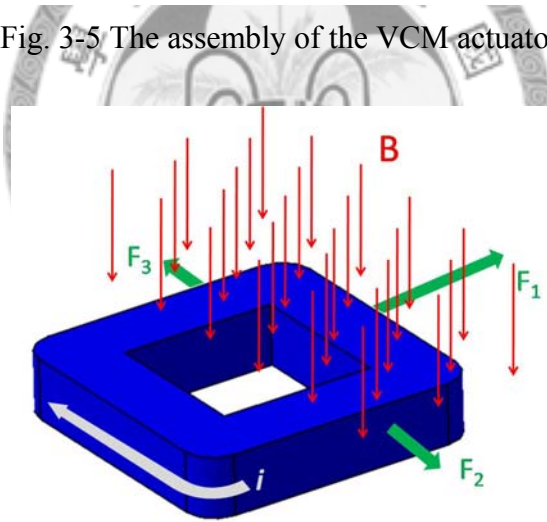
Fig. 3-6 The forces that are generated by Lorentz force principle

It is noteworthy that only half of the coil intersects the magnetic field, as shown

in Fig. 3-6. The part of the coil intersecting the magnetic field can actually be divided

into three sub-parts, which result in three corresponding electromagnetic forces, F_1, F_2

and F_3. Due to symmetry, the magnitudes of F_2 and F_3 are equal but the directions are

44

opposite. Since the two forces cancel each other, the effective force generated by the coil is only F_1. It is important to see that the magnitude of the effective force of a coil is invariant to the translation of the steel structure because the intersection part of the coil corresponding to F_1 is always constant and the varying forces F_2 and F_3 are always equal but opposite. When the stage rotates, the magnitudes of F_2 and F_3 are different. The purpose of the positioning stage is the precision motion in x- and y-axis, and the rotation angle of the stage is always regulated to zero. The difference of the magnitudes of F_2 and F_3 can be neglected when the rotation angle is small.

3.2.3 Eddy current damper

One should also beware the magnetic field intersects the copper mounting as well. When the steel structure and the magnetic field move relative to the copper mounting, the eddy current will be generated inside the copper structure. Hence, the interaction results in a damping force which resists the mentioned relative motion.
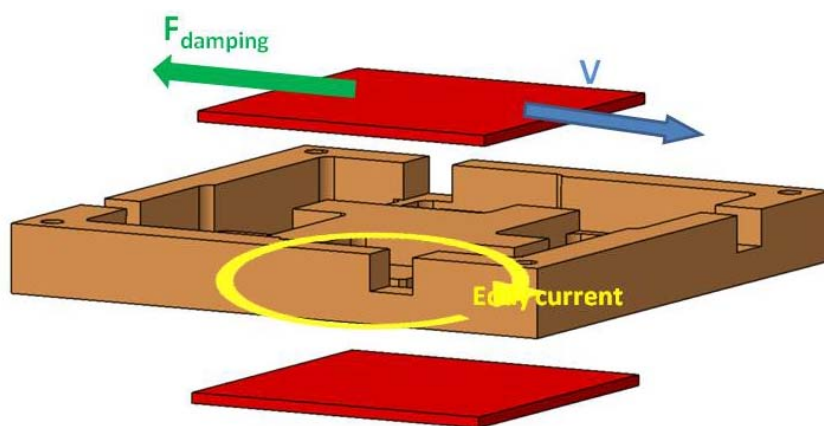
Fig. 3-7 The eddy current inside the copper mounting.

3.3　3-DOF Flexure Mechanism

Numerous multi-DOF flexure mechanisms have been presented in the literature. There are two well-known configurations adopted in the design of multi- DOF flexure stages – serial kinematics [20]-[25] and parallel kinematics [26]-[28]. Each configuration has its advantages and disadvantages.

In serial design, multiple DOFs are achieved by stacking multiple single DOF systems, one on another. The technical literature has presented several such designs. Serial kinematical mechanisms are relatively simple to design and have significantly higher inertia, but their weak points are the resulting center of gravity is relatively higher, and the off-axis errors are harder to be corrected. Besides those, the cables which are connected to every stage are sources of disturbance, which is detrimental for nanoscale positioning. Moreover, the actuators, especially when large range of motion is desired, are bulky and may reduce the motion bandwidth of the axes of DOF.

However, parallel kinematical designs are free of these problems due to ground mounted actuators, and are also usually more compact. On the other hand, they provide smaller ranges of motion and exhibit significant cross-axis coupling. Furthermore, the stiffness of one axis varies with motion or force along the other axis. This affects the

static as well as dynamic performance of the mechanism.

In our work, we use the parallel kinematical XY flexure mechanisms as shown in Fig. 3-8 and Fig. 3-9. The thin flexure mechanism is fabricated by electrical discharging wire cutting (EDWC), where the resulting height is 5mm and the width is only 0.3mm.
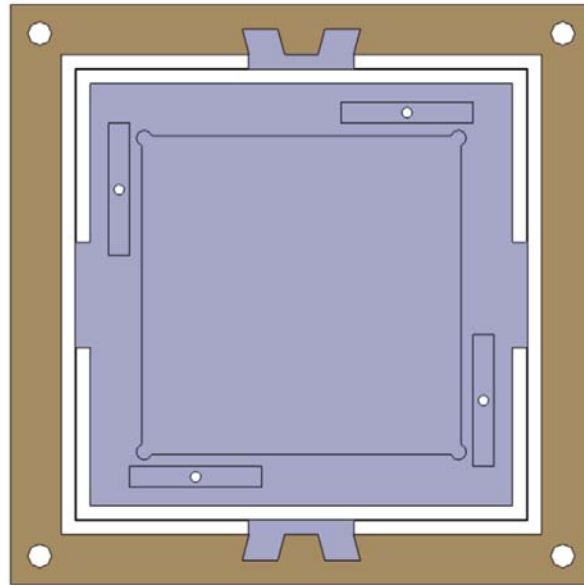
Fig. 3-8 Parallel kinematical XY flexure mechanism
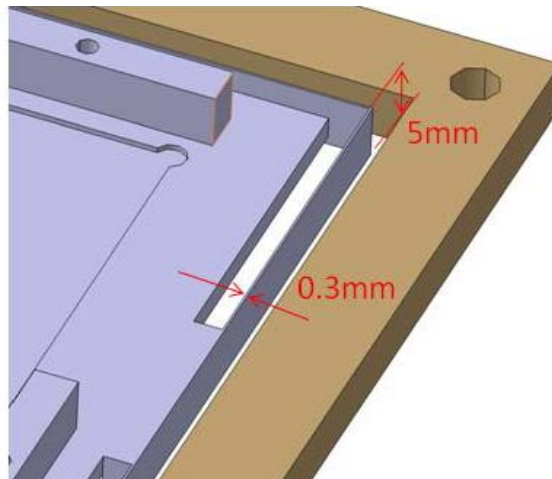
Fig. 3-9 The detailed view of the thin flexure

Note that the stiffness of the structure should be proportional to the area moment of inertia I. Recalling the cantilever as shown in Fig. 2-7, we can calculate the area moment of inertia I as:

$$I = \frac{bh^3}{12} \tag{3.1}$$

Since the height is greater than the width, the stiffness of our designed structure in vertical direction is much greater than that in the lateral direction. Therefore, we assume that the structure is always rigid in the vertical direction even when it has deformations in the lateral direction.
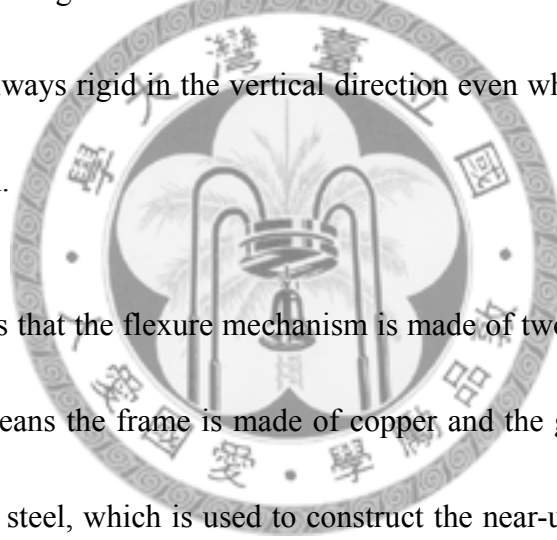
Figure 3-8 shows that the flexure mechanism is made of two kinds of material: the brown outer frame means the frame is made of copper and the gray blue inner flexure means the material is steel, which is used to construct the near-uniform magnetic field. The reason why the outer frame cannot be made of the same material as the inner flexure is that if the material of outer frame is also ferromagnetic, the moving stage will be attracted and stuck on the outer frame when it moves too close to the outer frame, as shown in Fig. 3-10. Thus, the outer frame should use non-ferromagnetic material. In our design, we choose copper as the material of the outer frame, and then the inner flexure is inlaid into the outer frame.
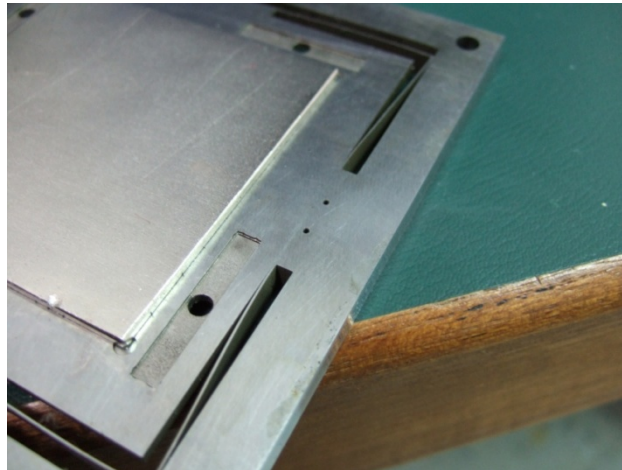
Fig. 3-10 The stiction on outer frame

3.4　Measurement System

In order to establish the control system of the 3-DOF positioning system, a 3-axis measurement scheme is proposed in this section. Three displacement sensors are placed coplanar with the moving stage to measure the position and posture of the stage. The model of sensors used in the proposed measurement system is OMRON Z4W series LED displacement sensor. The measurement principle of this sensor is based on triangulation methods, which is shown in Fig. 3-11. First, the light is emitted from the LED and then scatters from the surface of object. The scattering of the light will be focused on a position sensitive diode (PSD) inside the sensor. When the object displaces by dx, the focus spot on PSD will also displace by dy which is proportional to dx. Therefore, the displacement of the object can be measured from the output signal variation of PSD.
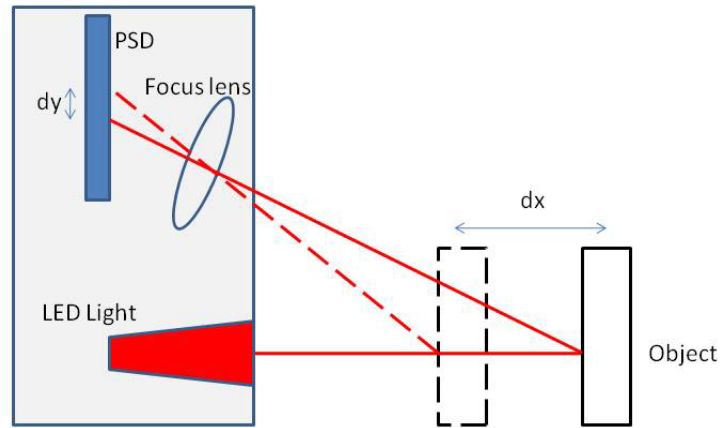
Fig. 3-11 The triangulation measurement method

The measurement metrology is shown in Fig. 3-12. One sensor is used to measure the displacement on the X-axis. On the other hands, two sensors are used to measure both the Y-axis displacement and the rotation angle θ of the positioning stage. Using this metrology, we can obtain the position and posture information of the positioning stage by the displacement information between the sensor and the scattering surface on the moving stage. The transformation from the measured signals to the real position and posture information of the positioning stage will be discussed in Section 4.2.
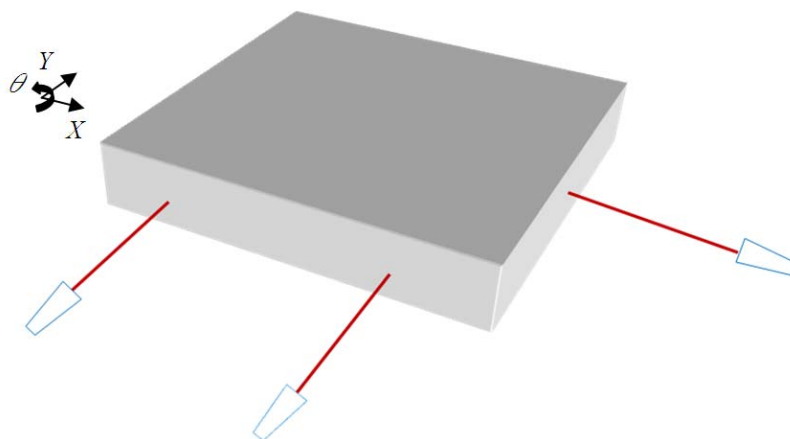
Fig. 3-12 Perspective view of the measuring system

3.5 Integrated Positioning Stage

In the previous sections in this chapter, we have discussed the design of electromagnetic actuators, damper, and the flexure suspension mechanism. Figure 3-13 shows the exploded view of the integrated positioning stage. The outer frames of upper and lower layer and the copper mounting are all fixed on the base layer, and then the entire positioning stage is fixed on a vibration-isolation table to reject the disturbance from the environment.
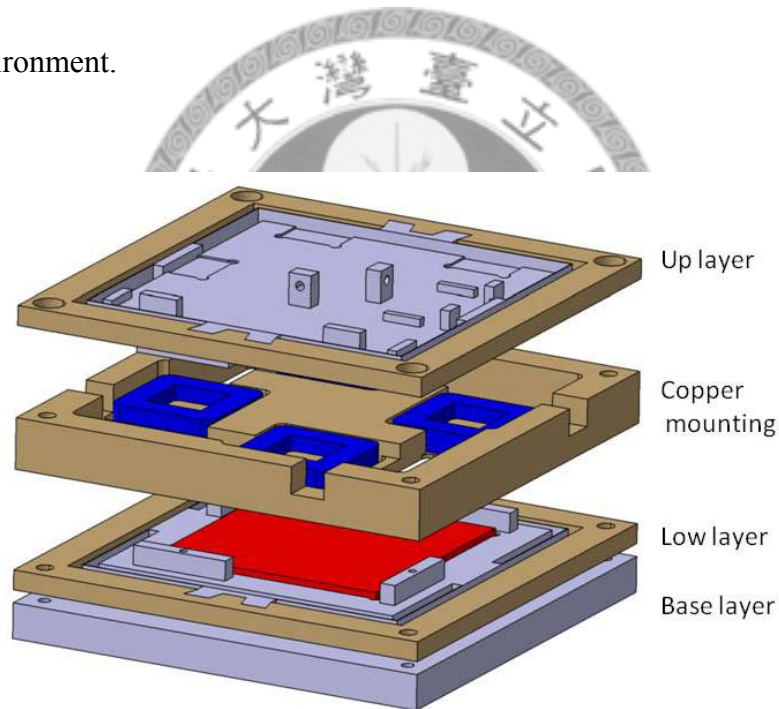
Fig. 3-13 The exploded view of the positioning stage

Since the center steel structure is suspended by the two layer flexure mechanism, so it is movable, and the allowed traveling range is 3mm x 3mm which is determined by the clearance between the steel structure and the copper mounting. Since the coils are fixed on the mounting and the steel structure is movable, the reacting forces of the

51

effective forces which have been mentioned before will act on the movable structure as

the propelling forces. With the four forces acting on the movable positioning stage as

shown in Fig. 3-14, the sum of the forces can drive the stages to move along x- and

y-axis and rotate along θ-axis.
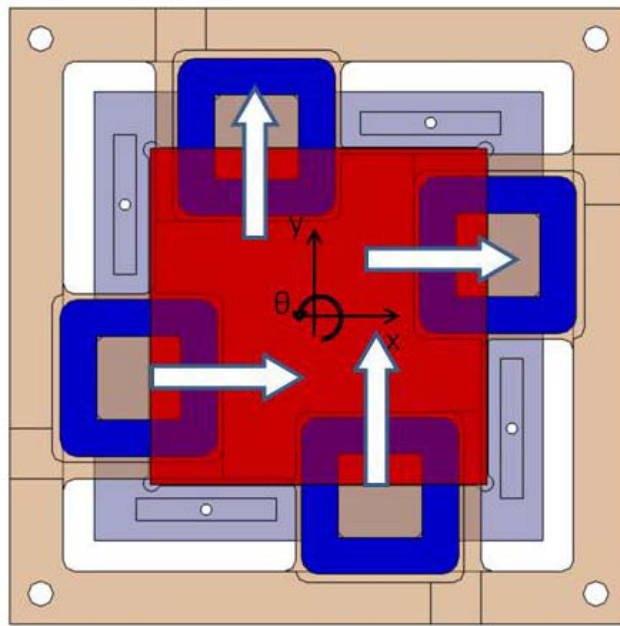
Fig. 3-14 The arrangement of four propelling forces

Note that all the forces, which include the reacting propelling forces and the

damping force, are located at the same positions while the movable structure is moving.

On the other hand, the arm between respective force exerting point to the center of mass

changes with the displacement of the movable stage. This phenomenon will result the

extra torque acting on the stage, but it can be overcome by careful force distribution.

Chapter 4
Modeling and System Identification

4.1　Force Allocation
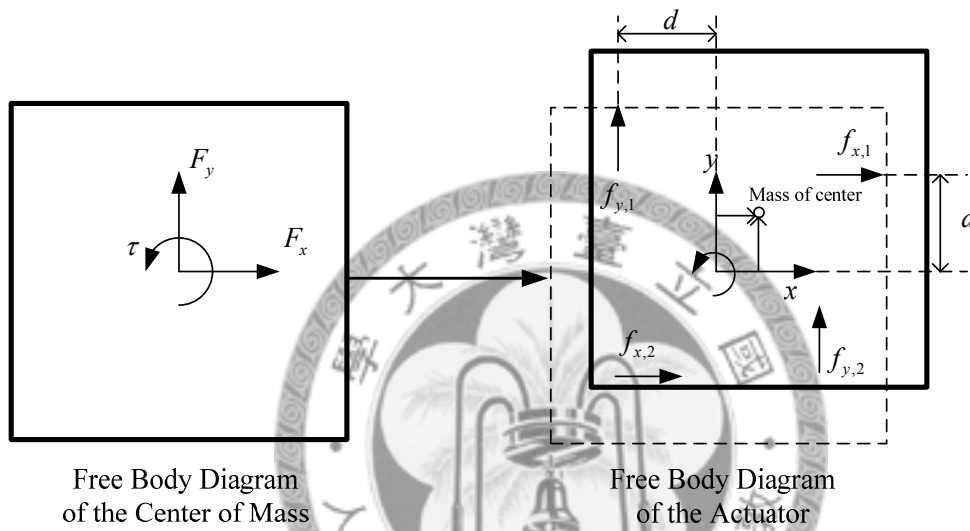
Fig. 4-1 The allocation of the forces

Referring to the end of last section, the arm of each force exertion to the center of mass changes with the displacement of the movable stage. As a result, an adequate force allocation strategy should be investigated to compensate the unexpected excessive torque. Figure 4-1 shows the force allocation. Let the arms of the four electromagnetic forces be the same d when the movable stage is located at the equilibrium. Consider the situation that the movable stage has displacements along both x- and y-axis, denote as x and y. The arms of the four forces are thus changed and the equation of the force

summation and the associated torque can be expressed as:

$$
\begin{aligned}
F_x &= f_{x,1} + f_{x,2} \\
F_y &= f_{y,1} + f_{y,2} \\
\tau &= f_{x,2} \cdot (d + y) - f_{x,1} \cdot (d - y) \\
&\quad + f_{y,2} \cdot (d - x) - f_{y,1} \cdot (d + x)
\end{aligned}
\tag{4.1}
$$

which can then be re-arranged into the following matrix form:

$$
\begin{bmatrix} F_x \\ F_y \\ \tau \end{bmatrix} =
\begin{bmatrix}
1 & 1 & 0 & 0 \\
0 & 0 & 1 & 1 \\
-d+y & d+y & -d-x & d-x
\end{bmatrix}
\begin{bmatrix} f_{x,1} \\ f_{x,2} \\ f_{y,1} \\ f_{y,2} \end{bmatrix}
\tag{4.2}
$$

A force allocation relationship should be established to distribute the control efforts to each electromagnetic actuator. From (4.2), the three control efforts are known and the four forces are unknown. This is an underdetermined linear system problem and the solution is not unique. A general solution can be expressed as:

$$
\begin{bmatrix} f_{x,1} \\ f_{x,2} \\ f_{y,1} \\ f_{y,2} \end{bmatrix} =
\left(
\begin{bmatrix}
\dfrac{d+y}{2d} & \dfrac{-d-x}{2d} & \dfrac{-1}{2d} \\
\dfrac{d-y}{2d} & \dfrac{d+x}{2d} & \dfrac{1}{2d} \\
0 & 1 & 0 \\
0 & 0 & 0
\end{bmatrix}
+
\begin{bmatrix} 1 \\ -1 \\ -1 \\ 1 \end{bmatrix} \mathbf{q}
\right)
\begin{bmatrix} F_x \\ F_y \\ \tau \end{bmatrix}
\tag{4.3}
$$

where $\mathbf{q}$ is an arbitrary vector. A trivial choice is $\mathbf{q} = [0\ 0\ 0]$. However the force allocation is inefficient because only $f_{x,1}$ and f_{x2} are used to generate torque and the $f_{y,2}$ is

54

redundant in (4.3). A carefully chosen **q** can decouple the forces along the x- and y-axis

and distribute current of each actuator more uniformly. A more adequate **q** is:

$$\mathbf{q} = \begin{bmatrix} 0 & \dfrac{d+x}{2d} & \dfrac{1}{4d} \end{bmatrix} \tag{4.4}$$

Substituting (4.4) into (4.3), we attain the following force allocation equation:

$$\begin{bmatrix} f_{x,1} \\ f_{x,2} \\ f_{y,1} \\ f_{y,2} \end{bmatrix} = \begin{bmatrix} \dfrac{d+y}{2d} & 0 & -\dfrac{1}{4d} \\ \dfrac{d-y}{2d} & 0 & \dfrac{1}{4d} \\ 0 & \dfrac{d-x}{2d} & -\dfrac{1}{4d} \\ 0 & \dfrac{d+x}{2d} & \dfrac{1}{4d} \end{bmatrix} \begin{bmatrix} F_x \\ F_y \\ \tau \end{bmatrix} \tag{4.5}$$

4.2 Sensing Methodology

Recall the measurement system mentioned in Section 3.4, in order to get the

position and posture information of the positioning stage, including the position in the

x- and y-axis and the rotating angle, three displacement sensors are used to measure

three distinct displacements of the positioning stage. Therefore, we appropriately

arrange the locations of the sensors. The proper arrangement of the sensors is illustrated

in Fig. 4-2.
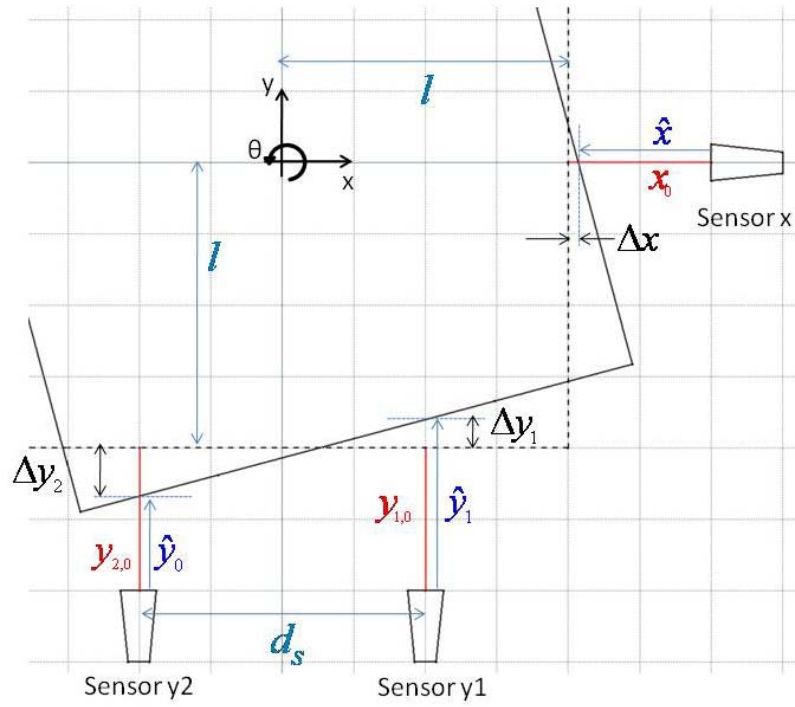
Fig. 4-2 The arrangement of sensors

The variables l and d_s mean the half width of the square moving stage and the distance between two sensors in y-axis, respectively. The measured distances of the three sensors are denoted as $\hat{x}, \hat{y}_1$ and $\hat{y}_2$. When the moving stage has no displacement and rotation, which is considered as equilibrium state, the constant distances are denoted as $x_0, y_{1,0}$ and $y_{2,0}$. Therefore, the differences of the distances can be expressed as:

$$\Delta x = x_0 - \hat{x}, \ \Delta y_1 = y_{1,0} - \hat{y}_1, \ \Delta y_2 = y_{2,0} - \hat{y}_2 \tag{4.6}$$

With the simple geometric relationships, the rotation of the moving stage can be expressed as:

$$\theta = \tan^{-1} \frac{\Delta y_1 - \Delta y_2}{d_s} \tag{4.7}$$

In Section 2.5, the error of measurement has been discussed. The compensation of the error should be considered in order to get accurate information about the position and posture of the positioning stage. In Fig. 4-2, even when the position of center of mass is kept at the origin, the measurement signals of sensors will still shift due to the rotation of the stage. The error is similar to cosine error. On the other hands, when there is a displacement of the moving stage in the y-axis as shown in Fig. 4-3, the Abbe error occurs because the motion axis and measurement axis are not in line.
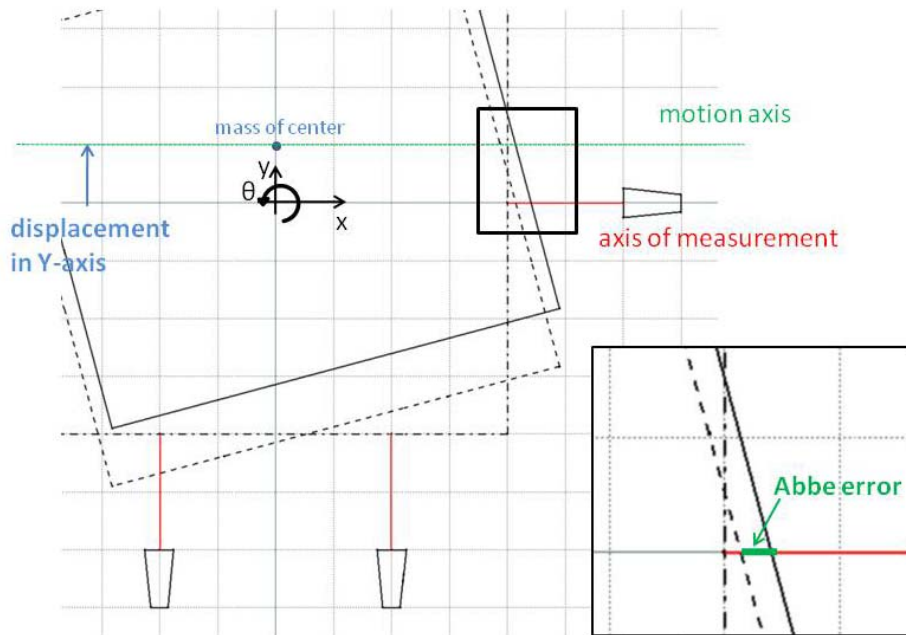
Fig. 4-3 Abbe error in the measurement system

Therefore, after compensation of Abbe error and cosine error terms, the position of the center of mass of the moving stage can be expressed as:

$$\begin{cases} x = -\Delta x - l\left(\sec\theta - 1\right) - y\tan\theta \\ y = \dfrac{\Delta y_1 + \Delta y_2}{2} - l\left(\sec\theta - 1\right) + x\tan\theta \end{cases}$$

(4.8)

where x and y are coupled in the above equation. To get a decoupled expression of position information, we rearrange some terms in (4.8) as follows:

$$\begin{cases} x + y\tan\theta = -\Delta x - l\left(\sec\theta - 1\right) \\ -x\tan\theta + y = \dfrac{\Delta y_1 + \Delta y_2}{2} - l\left(\sec\theta - 1\right) \end{cases}$$

$$\Rightarrow \begin{bmatrix} 1 & \tan\theta \\ -\tan\theta & 1 \end{bmatrix} \begin{bmatrix} x \\ y \end{bmatrix} = \begin{bmatrix} \Delta x - l\left(\sec\theta - 1\right) \\ \dfrac{\Delta y_1 + \Delta y_2}{2} - l\left(\sec\theta - 1\right) \end{bmatrix}$$

$$\Rightarrow \begin{bmatrix} x \\ y \end{bmatrix} = \begin{bmatrix} 1 & \tan\theta \\ -\tan\theta & 1 \end{bmatrix}^{-1} \begin{bmatrix} \Delta x - l\left(\sec\theta - 1\right) \\ \dfrac{\Delta y_1 + \Delta y_2}{2} - l\left(\sec\theta - 1\right) \end{bmatrix}$$

(4.9)

4.3 Dynamic Formulation

Figure 4-4 shows the free body diagram of the positioning system. The rigid body's dynamics of this positioning system are three degrees of freedom consisting of the translations in the x- and y-axis, respectively, and the rotation around the z-axis, defined as θ. Through the help of *Newton's Law,* the equations of motion can be expressed in the following equations:

$$\begin{aligned} m\ddot{x} &= F_x - k_x \cdot x - b_x \cdot \dot{x} \\ m\ddot{y} &= F_y - k_y \cdot y - b_y \cdot \dot{y} \\ J\ddot{\theta} &= \tau - k_\theta \cdot \theta - b_\theta \cdot \dot{\theta} - b_x \cdot \dot{x} \cdot y - b_y \cdot \dot{y} \cdot x \end{aligned}$$

(4.10)

58
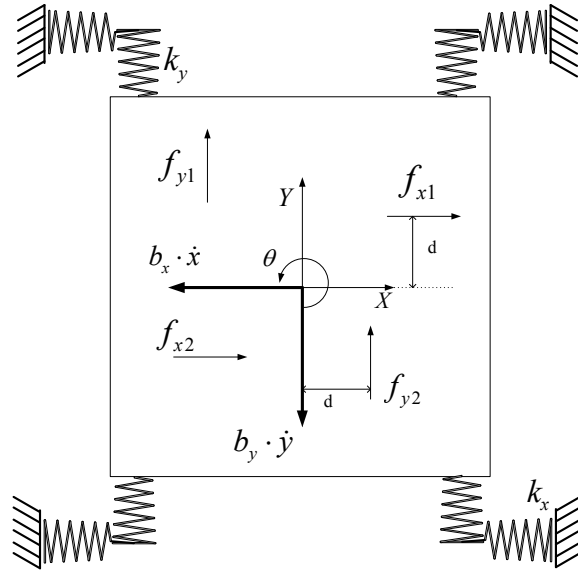
Fig. 4-4 The free body diagram of the system

where m is the mass of the moving stage, J is the moment of inertia, $k_{x/y/\theta}$ are the spring constants, $b_{x/y/\theta}$ are the damping constants, F_x, F_y, and τ are the control efforts which are mentioned in Section 4.1. Notice that the damping forces $b_x \cdot \dot{x}$ and $b_y \cdot \dot{y}$ are invariant to the motion of the mover. However, when the center of mass of the mover is not at the origin, the damping forces will cause unexpected torques $b_x \cdot \dot{x} \cdot y$ and $b_y \cdot \dot{y} \cdot x$ on the moving stage. To cancel the nonlinear terms, the feedback linearization is used. Define the control effort τ as:

$$\tau = \tau' + b_x \cdot \dot{x} \cdot y + b_y \cdot \dot{y} \cdot x \tag{4.11}$$

and substitute (4.11) into (4.10), then a linearized equation can be expressed as:

$$J\ddot{\theta} = \tau' - k_\theta \cdot \theta - b_\theta \cdot \dot{\theta} \tag{4.12}$$

59

To simplify the equation of motion, we define a variable vector as $\mathbf{x} = \begin{bmatrix} x & y & \theta \end{bmatrix}^T$ and reformulate the equation of motion into a matrix form:

$$\mathbf{M\ddot{x}} = \mathbf{Kx} + \mathbf{B\dot{x}} + \mathbf{U} \tag{4.13}$$

where $\mathbf{M}$ is the inertia matrix, $\mathbf{K}$ is the stiffness matrix, $\mathbf{B}$ is the damping matrix, and $\mathbf{U}$ is the control effort, which are defined as:

$$\mathbf{M} = \begin{bmatrix} m & 0 & 0 \\ 0 & m & 0 \\ 0 & 0 & J \end{bmatrix} \quad \mathbf{K} = \begin{bmatrix} k_x & 0 & 0 \\ 0 & k_y & 0 \\ 0 & 0 & k_\theta \end{bmatrix} \quad \mathbf{B} = \begin{bmatrix} b_x & 0 & 0 \\ 0 & b_y & 0 \\ 0 & 0 & b_\theta \end{bmatrix} \quad \mathbf{U} = \begin{bmatrix} F_x & F_y & \tau' \end{bmatrix}^T$$

4.4   System Identification

System identification is a very useful technique to build a mathematical model of a dynamic system based on measured input/output data. For the modern model-based control, knowing the characteristics of the system is essential to determine the design of controller. Some background knowledge of system identification by frequency response, which was referred to [29][30], will be briefly reviewed first. Then, the method will be applied to open-loop experiments to derive the mathematical model of the positioning system.

First, we will review the sweep frequency method in a view from frequency

domain. Considering a mass-spring with viscous damper, it corresponds to a standard 2nd order system whose equation of motion can be expressed as:

$$m\ddot{x} + b\dot{x} + kx = f(t) \qquad (4.14)$$

Let's define ω_n and ζ as :

$$\omega_n = \sqrt{\frac{k}{m}} \text{ , undamped natural frequency}$$

$$\zeta = \frac{b}{2\sqrt{mk}} \text{ , damping ratio} \qquad (4.15)$$

then by substituting (4.15) into (4.14) divided by m, we will obtain

$$\ddot{x} + 2\zeta\omega_n\dot{x} + \omega_n^2 x = \frac{f(t)}{m} \qquad (4.16)$$

If we assume that our forcing term is a sinusoidal function, then we will have

$$\ddot{x} + 2\zeta\omega_n\dot{x} + \omega_n^2 x = \frac{\overline{f}}{m}\sin(\omega t) \qquad (4.17)$$

From (4.17), we can find the magnitude of the system's transfer function, $|g(\omega)|$, as

$$|g(\omega)| \triangleq \frac{|\overline{x}|}{f} = \frac{1}{m\sqrt{(\omega_n^2 - \omega^2)^2 + (2\zeta\omega_n\omega)^2}} \qquad (4.18)$$

To test the dynamic property of the positioning system, sinusoidal signals with

manifold frequencies are fed into the system. From the input/output data, we can depict

the response in the frequency domain, as shown in Fig. 4-5. The way of finding the

damping ratio is to look for the half-power points of the response curve. By determining

the frequencies at which the amplitude of the response drops by a factor of $\sqrt{2}$ from

its peak value, we can then determine the damping ratio. According to Fig. 4-5, what we

now want is to determine the frequencies, ω_{h1} and ω_{h2}, at which he response amplitude

is equal to $\left|g(\omega_p)\right|/\sqrt{2}$. We will call the unknown half-power frequency ω_h.

Fig. 4-5 The frequency response of the standard 2nd order system

According to (4.18) and Fig. 4-5, for small damping ratio ($\zeta<0.05$), we can solve

the following equation to get the damping ratio of the system.

$$\frac{1}{m\sqrt{(\omega_n^2-\omega_h^2)^2+(2\zeta\omega_n\omega_h)^2}}=\frac{1}{\sqrt{2}}\cdot\frac{1}{m\cdot2\zeta\omega_n} \qquad (4.19)$$

After solving (4.19), we get

$$\omega_{h1} = -\zeta\omega_n + \omega_n\sqrt{1+\zeta^2}$$

$$\omega_{h2} = \zeta\omega_n + \omega_n\sqrt{1+\zeta^2} \tag{4.20}$$

and in turn

$$\omega_{h2} - \omega_{h1} = 2\zeta\omega_n \tag{4.21}$$

Let's define the bandwidth δ_h as

$$\delta_h \equiv \omega_{h2} - \omega_{h1}, \tag{4.22}$$

then, the damping ratio can readily be expressed as

$$\zeta = \frac{\delta_h}{2\omega_n} \tag{4.23}$$

In the sequel, we conduct the experiment of system identification on our system. We give a sinusoidal signal with sweeping frequencies from 1 Hz to 50Hz as forcing input and measure the system response, as shown in Figs. 4-6 and 4-7. These figures indicate that the resonant frequencies in the x-axis and the y-axis.

$$\omega_{nx} = 16.5 \ (\text{Hz}) = 2\pi \cdot 16.5 = 103.6726 \ (rad/s)$$

$$\omega_{ny} = 15.4 \ (\text{Hz}) = 2\pi \cdot 15.4 = 96.7611 \ (rad/s)$$

Besides, we also label the half-power frequencies from these figures. Using (4.22) and (4.23), we can get the damping ratio in the x-axis and y-axis, respectively, as follows :

$$\zeta_x = \frac{\delta_{hx}}{2\omega_{nx}} = \frac{\omega_{hx2} - \omega_{hx1}}{2\omega_{nx}} = \frac{30.495 - 30.082}{2 \cdot 16.5} = 0.0068$$

$$\zeta_y = \frac{\delta_{hy}}{2\omega_{ny}} = \frac{\omega_{hy2} - \omega_{hy1}}{2\omega_{ny}} = \frac{33.305 - 32.898}{2 \cdot 15.4} = 0.0062$$
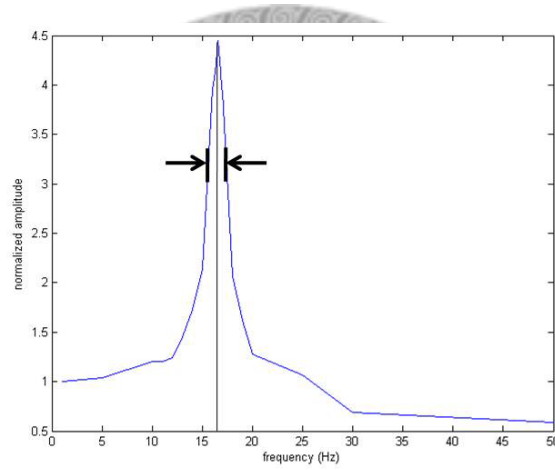
Fig. 4-6 Frequency response in the x-axis
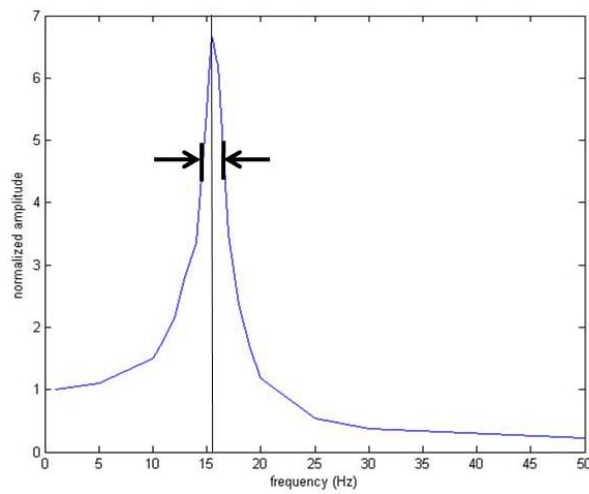
Fig. 4-7 Frequency response in the y-axis

Chapter 5　Controller Design

In order to achieve high positioning precision and reliable performance, a proper feedback controller is necessary for a positioning system. The system suffers from the measurement noise and external disturbance from the environment. Therefore, the desired controller should be robust enough to deal with these uncertainties and disturbances.

There are several kinds of available control methodologies, especially in the field of robust control [31][32], including H_∞ control [33], LQG control [34], sliding control [35]-[37], fuzzy control [38], backstepping control [39], and so on. For those methodologies, the controller gains are designed according to the nominal model. Although the resulting controller is sufficiently robust to the disturbance and can guarantee the stability, there still exist some drawbacks, and a major one is that the performance of positioning system may not meet our expectation perfectly because of the modeling error, say, due to simplification of the plant model.

Therefore, in order to design a controller which possesses not only stronger robustness but also self-tuning capability which can improve the performance, an advanced adaptive sliding mode control method has been proposed. In this section, we

first introduce the controller design as well as the stability analysis, and then present

some numerical simulations.

5.1   Adaptive Sliding Mode Controller Design

In general, the adaptive sliding mode controller belongs to the category of robust

control scheme. Here, the sliding mode controller can enable the positioning system to

possess strong robustness. On the other hand, the adaptive law can provide the on-line

estimation of the system parameters and then tune the controller gain to improve the

performance. Here, the adaptive scheme is classified as the direct adaptive control, as

shown in Fig. 5-1.
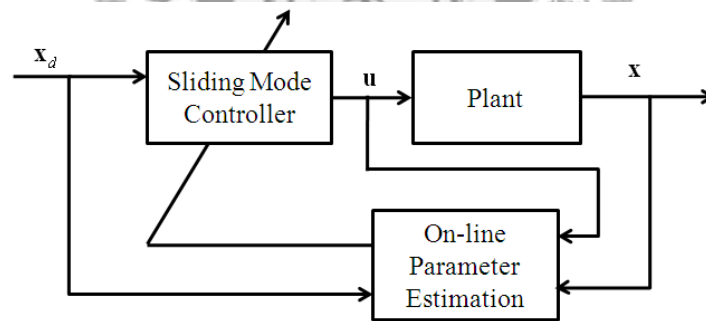
Fig. 5-1 Direct adaptive scheme

5.1.1   Problem statement

Before the formulation of the adaptive sliding mode controller, the plant model

should be stated again and the disturbance should be considered in the model. Recall the

equations of motion which is derived in Section 4.3 and add two uncertainty terms in

the model, namely,

$$\ddot{\mathbf{x}} = \mathbf{M}^{-1}\mathbf{K}\mathbf{x} + \mathbf{M}^{-1}\mathbf{B}\dot{\mathbf{x}} + \mathbf{M}^{-1}\mathbf{U} + \mathbf{w}_c + \mathbf{w}_v \tag{5.1}$$

where the constant uncertainty term $\mathbf{w}_c$ is denoted as the model uncertainty, and the variable uncertainty term $\mathbf{w}_v \equiv \begin{bmatrix} w_{v1} & w_{v2} & w_{v3} \end{bmatrix}^T$ is denoted as the external noise and disturbance subjected to the boundedness assumption $\|\mathbf{w}_v\| \leq \mathbf{w}_{max}$, which is defined as

$$\mathbf{w}_{max} \equiv \begin{bmatrix} w_{max,1} & w_{max,2} & w_{max,3} \end{bmatrix}^T$$

Define the desired states as $\mathbf{x}_d = \begin{bmatrix} x_d & y_d & \theta_d \end{bmatrix}^T$, and then the error vector between the desired states and system states can be expressed as:

$$\mathbf{e} = \mathbf{x}_d - \mathbf{x} = \begin{bmatrix} x_d - x & y_d - y & \theta_d - \theta \end{bmatrix}^T \tag{5.2}$$

which readily lead to the following dynamics:

$$\ddot{\mathbf{e}} = \mathbf{M}^{-1}\mathbf{K}\mathbf{x} + \mathbf{M}^{-1}\mathbf{B}\dot{\mathbf{x}} + \mathbf{M}^{-1}\mathbf{U} - \ddot{\mathbf{x}}_\mathbf{d} + \mathbf{w}_c + \mathbf{w}_v \tag{5.3}$$

To simplify the notation, define the $\mathbf{M}^{-1}\mathbf{K}$ as $\mathbf{K}_0$, $\mathbf{M}^{-1}\mathbf{B}$ as $\mathbf{B}_0$, $\mathbf{M}^{-1}$ as $\mathbf{M}_0$, so that, (5.3) can be expressed as:

$$\ddot{\mathbf{e}} = \mathbf{K}_0\mathbf{x} + \mathbf{B}_0\dot{\mathbf{x}} + \mathbf{M}_0\mathbf{U} - \ddot{\mathbf{x}}_\mathbf{d} + \mathbf{w}_c + \mathbf{w}_v \tag{5.4}$$

5.1.2 Sliding surface

Design a sliding surface $\mathbf{S}$, with the following form:

$$\mathbf{S} = \dot{\mathbf{e}} + \boldsymbol{\Lambda}\mathbf{e} \qquad (5.5)$$

where $\boldsymbol{\Lambda} = diag[\lambda_1 \quad \lambda_2 \quad \lambda_3]^T$ is a designed 3x3 positive diagonal matrix to be designed. From (5.5), we can very easily find that the sliding surface is a function consisting of the error vector and its time derivative. In this application, our main purpose is to regulate error vector to zero, which simultaneously regulates the time derivative to zero as well. If the sliding surface tends to zero within finite time, then $\mathbf{e}$ and its time derivative, $\dot{\mathbf{e}}$, are also forced to zero exponentially. To relate the sliding surface to the dynamics model, the time derivative of the sliding surface, $\dot{\mathbf{S}}$ can be expressed as:

$$\dot{\mathbf{S}} = \ddot{\mathbf{e}} + \boldsymbol{\Lambda}\dot{\mathbf{e}} \qquad (5.6)$$

After substituting (5.4) into (5.6), we rewrite $\dot{\mathbf{S}}$ as:

$$\dot{\mathbf{S}} = \mathbf{K}_0\mathbf{x} + \mathbf{B}_0\dot{\mathbf{x}} + \mathbf{M}_0\mathbf{U} - \ddot{\mathbf{x}}_d + \mathbf{w}_c + \mathbf{w}_v + \boldsymbol{\Lambda}\dot{\mathbf{e}} \qquad (5.7)$$

5.1.3 Adaptive sliding mode control law

68

As described in the previous section, a direct adaptive scheme is applied in this research, which is capable of estimating parameters of the system on-line and tuning the controller to improve the performance simultaneously. We can derive the control law based on the sliding surface dynamics according to the nominal plant model. Then, the estimations of system parameters will be substituted into the control law to replace the corresponding parameter. The adaptive sliding mode control law can be expressed as:

$$\mathbf{U} = \hat{\mathbf{M}}_0^{-1}\left(-\hat{\mathbf{K}}_0\mathbf{x} - \hat{\mathbf{B}}_0\dot{\mathbf{x}} + \ddot{\mathbf{x}}_d - \hat{\mathbf{w}}_c - \boldsymbol{\Lambda}\dot{\mathbf{e}} - \mathbf{Q}\mathbf{S} - \mathbf{N}sat(\mathbf{S})\right) \tag{5.8}$$

where $\mathbf{Q} = diag\begin{bmatrix} q_1 & q_2 & q_3 \end{bmatrix}^T$, $\forall k_i > 0$, $\mathbf{N} = diag\begin{bmatrix} \eta_1 & \eta_2 & \eta_3 \end{bmatrix}^T$, $\forall \eta_i > 0$, such that $\mathbf{N}$ stands for the high gain matrix used to bound the variable uncertainty $\mathbf{w}_v$, namely $\|\mathbf{N}\| \geq \mathbf{w}_{max}$, $\hat{\mathbf{M}}_0$, $\hat{\mathbf{K}}_0$, $\hat{\mathbf{B}}_0$, and $\hat{\mathbf{w}}_c$ are the estimates of $\mathbf{M}_0$, $\mathbf{K}_0$, $\mathbf{B}_0$, and $\mathbf{w}_c$ respectively, and $sat(.)$ is the saturation function defined as:

$$sat(\mathbf{S}) \equiv \begin{bmatrix} sat(s_1) & sat(s_2) & sat(s_3) \end{bmatrix}^T \tag{5.9}$$

where $sat(s_i) \equiv \begin{cases} 1 & s_i > \varepsilon_i \\ \dfrac{s_i}{\varepsilon_i} & if \quad -\varepsilon_i \leq s_i \leq \varepsilon_i \\ -1 & s_i < -\varepsilon_i \end{cases}$, $\mathbf{S} = \begin{bmatrix} s_1 & s_2 & s_3 \end{bmatrix}^T$, and $\boldsymbol{\varepsilon} \equiv \begin{bmatrix} \varepsilon_1 & \varepsilon_2 & \varepsilon_3 \end{bmatrix}^T > 0$

Notice that in the control effort $-\hat{\mathbf{B}}_0\dot{\mathbf{x}}$ is used to cancel the dynamic. The design counteracts the effect of the eddy current damper, which is used to increase the damping.

In theoretical view, if the system is modeled accurately enough, the vibration can be suppressed by the control effort. The actual stage is a high nonlinear system, but it is merely modeled by an over-simplified second-order system. Therefore, beside the control effort, the additional damper is needed in order to guarantee the plant is easier to be controlled.

5.1.4 Stability analysis

Choose the Lyapunov function candidate V, including the sliding variable and all estimated states in the system:

$$
\begin{aligned}
V &= \frac{1}{2}\mathbf{S}^T\mathbf{S} + \frac{1}{2}tr\left(\tilde{\mathbf{K}}_0^T\mathbf{\Gamma}_1^{-1}\tilde{\mathbf{K}}_0\right) + \frac{1}{2}tr\left(\tilde{\mathbf{B}}_0^T\mathbf{\Gamma}_2^{-1}\tilde{\mathbf{B}}_0\right) \\
&+ \frac{1}{2}tr\left(\tilde{\mathbf{M}}_0^T\mathbf{\Gamma}_3^{-1}\tilde{\mathbf{M}}_0\right) + \frac{1}{2}tr\left(\tilde{\mathbf{w}}_c^T\mathbf{\Gamma}_4^{-1}\tilde{\mathbf{w}}_c\right)
\end{aligned}
\tag{5.10}
$$

where $\mathbf{\Gamma}_1^{-1}$, $\mathbf{\Gamma}_2^{-1}$, $\mathbf{\Gamma}_3^{-1}$, and $\mathbf{\Gamma}_4^{-1}$ are all positive diagonal matrices, where $\mathbf{\Gamma}_i = diag[\gamma_{i1}\ \gamma_{i2}\ \gamma_{i3}]^T$ $\forall i=1,2,3$, tr(.) is the trace of a matrix. $\tilde{\mathbf{K}}_0, \tilde{\mathbf{B}}_0, \tilde{\mathbf{M}}_0$, and $\tilde{\mathbf{w}}_c$ are the estimation errors, respectively, defined as $\tilde{\mathbf{K}}_0 = \hat{\mathbf{K}}_0 - \mathbf{K}_0$, $\tilde{\mathbf{B}}_0 = \hat{\mathbf{B}}_0 - \mathbf{B}_0$, $\tilde{\mathbf{M}}_0 = \hat{\mathbf{M}}_0 - \mathbf{M}_0$, and $\tilde{\mathbf{w}}_c = \hat{\mathbf{w}}_c - \mathbf{w}_c$.

The time derivative of the Lyapunov function candidate apparently is:

$$
\dot{V} = \mathbf{S}^T\dot{\mathbf{S}} + tr\left(\tilde{\mathbf{K}}_0^T\mathbf{\Gamma}_1^{-1}\dot{\hat{\mathbf{K}}}_0\right) + tr\left(\tilde{\mathbf{B}}_0^T\mathbf{\Gamma}_2^{-1}\dot{\hat{\mathbf{B}}}_0\right) + tr\left(\tilde{\mathbf{M}}_0^T\mathbf{\Gamma}_3^{-1}\dot{\hat{\mathbf{M}}}_0\right) + tr\left(\tilde{\mathbf{w}}_c^T\mathbf{\Gamma}_4^{-1}\dot{\hat{\mathbf{w}}}_c\right)
\tag{5.11}
$$

Recalling (5.7) and substituting the adaptive control law into the time derivative of the sliding variable, the resulting equation can be expressed as:

$$\dot{\mathbf{S}} = \mathbf{K}_0\mathbf{x} + \mathbf{B}_0\dot{\mathbf{x}} + \mathbf{M}_0\hat{\mathbf{M}}_0^{-1}\left(-\hat{\mathbf{K}}_0\mathbf{x} - \hat{\mathbf{B}}_0\dot{\mathbf{x}} + \ddot{\mathbf{x}}_d - \hat{\mathbf{w}}_c - \boldsymbol{\Lambda}\dot{\mathbf{e}} - \mathbf{QS} - \mathbf{N}sat(\mathbf{S})\right)$$
$$- \ddot{\mathbf{x}}_d + \mathbf{w}_c + \mathbf{w}_v + \boldsymbol{\Lambda}\dot{\mathbf{e}}$$

$$\dot{\mathbf{S}} = \mathbf{K}_0\mathbf{x} + \mathbf{B}_0\dot{\mathbf{x}} + (\hat{\mathbf{M}}_0 - \tilde{\mathbf{M}}_0)\hat{\mathbf{M}}_0^{-1}\left(-\hat{\mathbf{K}}_0\mathbf{x} - \hat{\mathbf{B}}_0\dot{\mathbf{x}} + \ddot{\mathbf{x}}_d - \hat{\mathbf{w}}_c - \boldsymbol{\Lambda}\dot{\mathbf{e}} - \mathbf{QS} - \mathbf{N}sat(\mathbf{S})\right)$$
$$- \ddot{\mathbf{x}}_d + \mathbf{w}_c + \mathbf{w}_v + \boldsymbol{\Lambda}\dot{\mathbf{e}}$$

$$\dot{\mathbf{S}} = -\tilde{\mathbf{M}}_0\mathbf{U} - \tilde{\mathbf{K}}_0\mathbf{x} - \tilde{\mathbf{B}}_0\dot{\mathbf{x}} - \tilde{\mathbf{w}}_c - \mathbf{QS} - \mathbf{N}sat(\mathbf{S}) + \mathbf{w}_v \qquad (5.12)$$

Then, after substitution of (5.12) into (5.11), the time derivative of V will become:

$$\dot{V} = \mathbf{S}^T\left(-\tilde{\mathbf{M}}_0\mathbf{U} - \tilde{\mathbf{K}}_0\mathbf{x} - \tilde{\mathbf{B}}_0\dot{\mathbf{x}} - \tilde{\mathbf{w}}_c - \mathbf{QS} - \mathbf{N}sat(\mathbf{S}) + \mathbf{w}_v\right)$$
$$+ tr\left(\tilde{\mathbf{K}}_0^T\boldsymbol{\Gamma}_1^{-1}\dot{\hat{\mathbf{K}}}_0\right) + tr\left(\tilde{\mathbf{B}}_0^T\boldsymbol{\Gamma}_2^{-1}\dot{\hat{\mathbf{B}}}_0\right) + tr\left(\tilde{\mathbf{M}}_0^T\boldsymbol{\Gamma}_3^{-1}\dot{\hat{\mathbf{M}}}_0\right) + tr\left(\tilde{\mathbf{w}}_c^T\boldsymbol{\Gamma}_4^{-1}\dot{\hat{\mathbf{w}}}_c\right)$$
$$= -\mathbf{S}^T\mathbf{QS} - \mathbf{S}^T\left(\mathbf{N}sat(\mathbf{S}) - \mathbf{w}_v\right) - \mathbf{S}^T\left(-\tilde{\mathbf{M}}_0\mathbf{U} - \tilde{\mathbf{K}}_0\mathbf{x} - \tilde{\mathbf{B}}_0\dot{\mathbf{x}} - \tilde{\mathbf{w}}_c\right)$$
$$+ tr\left(\tilde{\mathbf{K}}_0^T\boldsymbol{\Gamma}_1^{-1}\dot{\hat{\mathbf{K}}}_0\right) + tr\left(\tilde{\mathbf{B}}_0^T\boldsymbol{\Gamma}_2^{-1}\dot{\hat{\mathbf{B}}}_0\right) + tr\left(\tilde{\mathbf{M}}_0^T\boldsymbol{\Gamma}_3^{-1}\dot{\hat{\mathbf{M}}}_0\right) + tr\left(\tilde{\mathbf{w}}_c^T\boldsymbol{\Gamma}_4^{-1}\dot{\hat{\mathbf{w}}}_c\right) \qquad (5.13)$$

In order to simplify (5.13), the trace operations are used, which include:

a. $tr(AB) = tr(BA)$, for any $A, B \in R^{n \times n}$;
b. $tr(A+B) = tr(B+A)$, for any $A, B \in R^{n \times n}$;
c. $tr(xy^T) = tr(yx^T) = x^Ty = y^Tx$, for any $x, y \in R^{n \times l}$.

A group of terms in (5.13) can be rewritten as:

$$\mathbf{S}^T\left(\tilde{\mathbf{M}}_0\mathbf{U} + \tilde{\mathbf{K}}_0\mathbf{x} + \tilde{\mathbf{B}}_0\dot{\mathbf{x}} + \tilde{\mathbf{w}}_c\right)$$
$$= tr\left[\mathbf{S}\left(\tilde{\mathbf{M}}_0\mathbf{U} + \tilde{\mathbf{K}}_0\mathbf{x} + \tilde{\mathbf{B}}_0\dot{\mathbf{x}} + \tilde{\mathbf{w}}_c\right)^T\right]$$
$$= tr\left(\mathbf{S}\mathbf{U}^T\tilde{\mathbf{M}}_0^T + \mathbf{S}\mathbf{x}^T\tilde{\mathbf{K}}_0^T + \mathbf{S}\dot{\mathbf{x}}^T\tilde{\mathbf{B}}_0^T + \mathbf{S}\tilde{\mathbf{w}}_c^T\right)$$
$$= tr\left(\tilde{\mathbf{M}}_0^T\mathbf{S}\mathbf{U}^T + \tilde{\mathbf{K}}_0^T\mathbf{S}\mathbf{x}^T + \tilde{\mathbf{B}}_0^T\mathbf{S}\dot{\mathbf{x}}^T + \tilde{\mathbf{w}}_c^T\mathbf{S}\right)$$
$$= tr\left(\tilde{\mathbf{M}}_0^T\mathbf{S}\mathbf{U}^T\right) + tr\left(\tilde{\mathbf{K}}_0^T\mathbf{S}\mathbf{x}^T\right) + tr\left(\tilde{\mathbf{B}}_0^T\mathbf{S}\dot{\mathbf{x}}^T\right) + tr\left(\tilde{\mathbf{w}}_c^T\mathbf{S}\right) \qquad (5.14)$$

Accordingly, (5.13) can be simplified as:

$$\dot{V} = -\mathbf{S}^T\mathbf{Q}\mathbf{S} - \mathbf{S}^T\left(\mathbf{N}sat(\mathbf{S}) - \mathbf{w}_v\right)$$
$$+ tr\left[\tilde{\mathbf{K}}_0^T\left(\boldsymbol{\Gamma}_1^{-1}\dot{\hat{\mathbf{K}}}_0 + \mathbf{S}\mathbf{x}^T\right)\right] + tr\left[\tilde{\mathbf{B}}_0^T\left(\boldsymbol{\Gamma}_2^{-1}\dot{\hat{\mathbf{B}}}_0 + \mathbf{S}\dot{\mathbf{x}}^T\right)\right] \quad (5.15)$$
$$+ tr\left[\tilde{\mathbf{M}}_0^T\left(\boldsymbol{\Gamma}_3^{-1}\dot{\hat{\mathbf{M}}}_0 + \mathbf{S}\mathbf{U}^T\right)\right] + tr\left[\tilde{\mathbf{w}}_c^T\left(\boldsymbol{\Gamma}_4^{-1}\dot{\hat{\mathbf{w}}}_c + \mathbf{S}\right)\right]$$

Now, the adaptive law can be chosen as:

$$\dot{\hat{\mathbf{K}}}_0 = \dot{\tilde{\mathbf{K}}}_0 = -\boldsymbol{\Gamma}_1\mathbf{S}\mathbf{x}^T - \boldsymbol{\Gamma}_1\boldsymbol{\Sigma}_1\hat{\mathbf{K}}_0$$
$$\dot{\hat{\mathbf{B}}}_0 = \dot{\tilde{\mathbf{B}}}_0 = -\boldsymbol{\Gamma}_2\mathbf{S}\dot{\mathbf{x}}^T - \boldsymbol{\Gamma}_2\boldsymbol{\Sigma}_2\hat{\mathbf{B}}_0$$
$$\dot{\hat{\mathbf{M}}}_0 = \dot{\tilde{\mathbf{M}}}_0 = -\boldsymbol{\Gamma}_3\mathbf{S}\mathbf{U}^T - \boldsymbol{\Gamma}_3\boldsymbol{\Sigma}_3\hat{\mathbf{M}}_0 \quad (5.16)$$
$$\dot{\hat{\mathbf{w}}}_c = \dot{\tilde{\mathbf{w}}}_c = -\boldsymbol{\Gamma}_4\mathbf{S} - \boldsymbol{\Gamma}_4\boldsymbol{\Sigma}_4\hat{\mathbf{w}}_c$$

where $\boldsymbol{\Sigma}_1$, $\boldsymbol{\Sigma}_2$, $\boldsymbol{\Sigma}_3$, and $\boldsymbol{\Sigma}_4$ are all 3x3 positive diagonal matrices chosen by the designer, namely, $\boldsymbol{\Sigma}_i = diag\begin{bmatrix}\sigma_{i1} & \sigma_{i2} & \sigma_{i3}\end{bmatrix}^T \quad \forall i=1,2,3$.

By substituting the adaptive law (5.16) into (5.15), we see that the time derivative of V can be expressed as:

$$\dot{V} = -\mathbf{S}^T\mathbf{Q}\mathbf{S} - \mathbf{S}^T\left(\mathbf{N}sat(\mathbf{S}) - \mathbf{w}_v\right)$$
$$- tr\left[\tilde{\mathbf{K}}_0^T\boldsymbol{\Sigma}_1\hat{\mathbf{K}}_0\right] - tr\left[\tilde{\mathbf{B}}_0^T\boldsymbol{\Sigma}_2\hat{\mathbf{B}}_0\right] - tr\left[\tilde{\mathbf{M}}_0^T\boldsymbol{\Sigma}_3\hat{\mathbf{M}}_0\right] - tr\left[\tilde{\mathbf{w}}_c^T\boldsymbol{\Sigma}_4\hat{\mathbf{w}}_c\right]$$
$$= -\mathbf{S}^T\mathbf{Q}\mathbf{S} - \mathbf{S}^T\left(\mathbf{N}sat(\mathbf{S}) - \mathbf{w}_v\right)$$
$$- \sum_{j=1}^{3}(\sigma_{1j}\tilde{k}_{0j}{}^T\hat{k}_{0j} + \sigma_{2j}\tilde{b}_{0j}{}^T\hat{b}_{0j} + \sigma_{3j}\tilde{m}_{0j}{}^T\hat{m}_{0j} + \sigma_{4j}\tilde{w}_{cj}{}^T\hat{w}_{cj}) \quad (5.17)$$

Then, we adapt the following inequality

$$-\sigma_{1j}\tilde{k}_{0j}{}^{T}\hat{k}_{0j} = -\sigma_{1j}\tilde{k}_{0j}{}^{T}\left(\tilde{k}_{0j}+k_{0j}\right)$$

$$\leq -\sigma_{1j}\left\|\tilde{k}_{0j}\right\|^{2}+\sigma_{1j}\left\|\tilde{k}_{0j}\right\|\cdot\left\|k_{0j}\right\| \tag{5.18}$$

Using completion of squares, we can rewrite the above as:

$$-\sigma_{1j}\left\|\tilde{k}_{0j}\right\|^{2}+\sigma_{1j}\left\|\tilde{k}_{0j}\right\|\cdot\left\|k_{0j}\right\| \leq -\frac{\sigma_{1j}}{2}\left\|\tilde{k}_{0j}\right\|^{2}-\frac{\sigma_{1j}}{2}\left(\left\|\tilde{k}_{0j}\right\|-\left\|k_{0j}\right\|\right)^{2}+\frac{\sigma_{1j}}{2}\left\|k_{0j}\right\|^{2}$$

$$\leq -\frac{\sigma_{1j}}{2}\left\|\tilde{k}_{0j}\right\|^{2}+\frac{\sigma_{1j}}{2}\left\|k_{0j}\right\|^{2} \tag{5.19}$$

By combining inequalities (5.18) and (5.19), we therefore can obtain the result of

inequality as follows:

$$-\sigma_{1j}\tilde{k}_{0j}{}^{T}\hat{k}_{0j} \leq -\frac{\sigma_{1j}}{2}\left\|\tilde{k}_{0j}\right\|^{2}+\frac{\sigma_{1j}}{2}\left\|k_{0j}\right\|^{2}=-\frac{\sigma_{1j}}{2}\left[\left\|\tilde{k}_{0j}\right\|^{2}-\left\|k_{0j}\right\|^{2}\right] \tag{5.20}$$

Similar to inequality (5.20), we can obtain the following inequalities as well:

$$-\sigma_{2j}\tilde{b}_{0j}{}^{T}\hat{b}_{0j} \leq -\frac{\sigma_{2j}}{2}\left[\left\|\tilde{b}_{0j}\right\|^{2}-\left\|b_{0j}\right\|^{2}\right],$$

$$-\sigma_{3j}\tilde{m}_{0j}{}^{T}\hat{m}_{0j} \leq -\frac{\sigma_{3j}}{2}\left[\left\|\tilde{m}_{0j}\right\|^{2}-\left\|m_{0j}\right\|^{2}\right], \tag{5.21}$$

$$-\sigma_{4j}\tilde{w}_{cj}{}^{T}\hat{w}_{cj} \leq -\frac{\sigma_{4j}}{2}\left[\left\|\tilde{w}_{cj}\right\|^{2}-\left\|w_{cj}\right\|^{2}\right].$$

Finally, we take inequalities (5.20) and (5.21) into (5.17) so that we can obtain

$$\dot{V} \leq -\mathbf{S}^T \mathbf{Q} \mathbf{S} - \mathbf{S}^T \left(\mathbf{N} sat(\mathbf{S}) - \mathbf{w}_v \right)$$
$$-\sum_{j=1}^{3} \left\{ \begin{matrix} \frac{\sigma_{1j}}{2} \left[\left\| \tilde{k}_{0j} \right\|^2 - \left\| k_{0j} \right\|^2 \right] + \frac{\sigma_{2j}}{2} \left[\left\| \tilde{b}_{0j} \right\|^2 - \left\| b_{0j} \right\|^2 \right] \\ + \frac{\sigma_{3j}}{2} \left[\left\| \tilde{m}_{0j} \right\|^2 - \left\| m_{0j} \right\|^2 \right] + \frac{\sigma_{4j}}{2} \left[\left\| \tilde{w}_{cj} \right\|^2 - \left\| w_{cj} \right\|^2 \right] \end{matrix} \right\} \tag{5.22}$$

If we choose $0 < \alpha < \min\left\{ 2q_j, \ \gamma_{1j}\sigma_{1j}, \ \gamma_{2j}\sigma_{2j}, \ \gamma_{3j}\sigma_{3j}, \ \gamma_{4j}\sigma_{4j} \right\}, \forall j = 1 \sim 3$, we can then

obtain the following equation:

$$\dot{V} \leq -\mathbf{S}^T \left(\mathbf{N} sat(\mathbf{S}) - \mathbf{w}_v \right)$$
$$-\alpha V + \sum_{j=1}^{3} \left\{ \frac{\sigma_{1j}}{2} \left\| k_{0j} \right\|^2 + \frac{\sigma_{2j}}{2} \left\| b_{0j} \right\|^2 + \frac{\sigma_{3j}}{2} \left\| m_{0j} \right\|^2 + \frac{\sigma_{4j}}{2} \left\| w_{cj} \right\|^2 \right\} \tag{5.23}$$

Since all the matrixes of the first term in (5.23) are diagonal, the above equation

can be rewritten as:

$$\dot{V} \leq -\sum_{i=1}^{3} s_i \left[\eta_i sat(s_i) - w_{vi} \right]$$
$$-\alpha V + \sum_{j=1}^{3} \left\{ \frac{\sigma_{1j}}{2} \left\| k_{0j} \right\|^2 + \frac{\sigma_{2j}}{2} \left\| b_{0j} \right\|^2 + \frac{\sigma_{3j}}{2} \left\| m_{0j} \right\|^2 + \frac{\sigma_{4j}}{2} \left\| w_{cj} \right\|^2 \right\} \tag{5.24}$$

Because the sliding mode control scheme involving saturation function belongs to

boundary layer control, the analysis should be considered in two situations. First,

considering the sliding variables are outside the boundary layer, the saturation function

can be readily replaced by the sign function. Take the first element of the first term in

(5.24) as the example:

74

$$s_1 \left[\eta_1 sat(s_1) - w_{v1} \right] = s_1 \left[\eta_1 \operatorname{sgn}(s_1) - w_{v1} \right] = s_1 \left[\eta_1 \frac{\|s_1\|}{s_1} - w_{v1} \right] = \|s_1\| \eta_1 - s_1 w_{v1}$$

(5.25)

By substituting the upper bound $w_{\max,1}$ into (5.25), we can obtain the following

inequality:

$$s_1 \left[\eta_1 sat(s_1) - w_{v1} \right] \geq \|s_1\| \eta_1 - \|s_1\| w_{\max,1} = \|s_1\| \left(\eta_1 - w_{\max,1} \right)$$

(5.26)

Similar to inequality (5.26), we can obtain the following inequalities as well:

$$s_2 \left[\eta_2 sat(s_3) - w_{v3} \right] \geq \|s_2\| \left(\eta_2 - w_{\max,2} \right)$$
$$s_3 \left[\eta_3 sat(s_3) - w_{v3} \right] \geq \|s_3\| \left(\eta_3 - w_{\max,3} \right)$$

(5.27)

After the substitution of the inequalities (5.26) and (5.27) into (5.24), the time derivative

of V can be rewritten as:

$$\dot{V} \leq -\sum_{i=1}^{3} \|s_i\| \left(\eta_i - w_{\max,i} \right)$$
$$- \alpha V + \sum_{j=1}^{3} \left\{ \frac{\sigma_{1j}}{2} \|k_{0j}\|^2 + \frac{\sigma_{2j}}{2} \|b_{0j}\|^2 + \frac{\sigma_{3j}}{2} \|m_{0j}\|^2 + \frac{\sigma_{4j}}{2} \|w_{cj}\|^2 \right\}$$

(5.28)

Since $\eta_i - w_{\max,i} > 0$, $\forall i = 1, 2, 3$, (5.28) will become:

$$\dot{V} \leq -\alpha V + \sum_{j=1}^{3} \left\{ \frac{\sigma_{1j}}{2} \|k_{0j}\|^2 + \frac{\sigma_{2j}}{2} \|b_{0j}\|^2 + \frac{\sigma_{3j}}{2} \|m_{0j}\|^2 + \frac{\sigma_{4j}}{2} \|w_{cj}\|^2 \right\}$$

(5.29)

Second, considering the sliding variables are inside the boundary layer, the saturation function will replaced by s_i / ε_i. Take the first element of the first term in (5.24) as the example:

$$
\begin{aligned}
s_1 \left[\eta_1 sat(s_1) - w_{v1} \right] &= s_1 \left[\eta_1 \frac{s_1}{\varepsilon_1} - w_{v1} \right] = \frac{\eta_1}{\varepsilon_1} s_1^2 - w_{v1} s_1 \\
&\geq \frac{\eta_1}{\varepsilon_1} \|s_1\|^2 - w_{max,1} \|s_1\|
\end{aligned}
\tag{5.30}
$$

Using completion of squares, we can rewrite the above as:

$$
\begin{aligned}
s_1 \left[\eta_1 sat(s_1) - w_{v1} \right] &\geq \frac{\eta_1}{\varepsilon_1} \|s_1\|^2 - w_{max,1} \|s_1\| + \frac{\varepsilon_1}{4\eta_1} w_{max,1}^2 - \frac{\varepsilon_1}{4\eta_1} w_{max,1}^2 \\
&\geq \left(\sqrt{\frac{\eta_1}{\varepsilon_1}} \|s_1\| - \frac{1}{2} \sqrt{\frac{\varepsilon_1}{\eta_1}} w_{max,1} \right)^2 - \frac{\varepsilon_1}{4\eta_1} w_{max,1}^2
\end{aligned}
\tag{5.31}
$$

Similar to inequality (5.31), we can obtain the following inequalities as well:

$$
\begin{aligned}
s_2 \left[\eta_2 sat(s_2) - w_{v2} \right] &\geq \left(\sqrt{\frac{\eta_2}{\varepsilon_2}} \|s_2\| - \frac{1}{2} \sqrt{\frac{\varepsilon_2}{\eta_2}} w_{max,2} \right)^2 - \frac{\varepsilon_2}{4\eta_2} w_{max,2}^2 \\
s_3 \left[\eta_3 sat(s_3) - w_{v3} \right] &\geq \left(\sqrt{\frac{\eta_3}{\varepsilon_3}} \|s_3\| - \frac{1}{2} \sqrt{\frac{\varepsilon_3}{\eta_3}} w_{max,3} \right)^2 - \frac{\varepsilon_3}{4\eta_3} w_{max,3}^2
\end{aligned}
\tag{5.32}
$$

After the substitution of the inequalities (5.31) and (5.32) into (5.24), the time derivative of V can be rewritten as:

$$\dot{V} \le -\sum_{j=1}^{3}\left[\left(\sqrt{\frac{\eta_j}{\varepsilon_j}}\left\|s_j\right\| - \frac{1}{2}\sqrt{\frac{\varepsilon_j}{\eta_j}}w_{\max,j}\right)^2 - \frac{\varepsilon_j}{4\eta_j}w_{\max,j}^2\right]$$

$$-\alpha V + \sum_{j=1}^{3}\left\{\frac{\sigma_{1j}}{2}\left\|k_{0j}\right\|^2 + \frac{\sigma_{2j}}{2}\left\|b_{0j}\right\|^2 + \frac{\sigma_{3j}}{2}\left\|m_{0j}\right\|^2 + \frac{\sigma_{4j}}{2}\left\|w_{cj}\right\|^2\right\}$$

$$\le -\alpha V + \sum_{j=1}^{3}\left\{\frac{\varepsilon_j}{4\eta_j}w_{\max,j}^2 + \frac{\sigma_{1j}}{2}\left\|k_{0j}\right\|^2 + \frac{\sigma_{2j}}{2}\left\|b_{0j}\right\|^2 + \frac{\sigma_{3j}}{2}\left\|m_{0j}\right\|^2 + \frac{\sigma_{4j}}{2}\left\|w_{cj}\right\|^2\right\} \quad (5.33)$$

After considering the above two situations, we can conclude the most conservative bounded stability:

$$\dot{V} \le 0 \quad \text{when} \quad V \ge V_0 = \frac{1}{2\alpha}\sum_{j=1}^{3}\left\{\frac{\varepsilon_j}{2\eta_j}w_{\max,j}^2 + \sigma_{1j}\left\|k_{0j}\right\|^2 + \sigma_{2j}\left\|b_{0j}\right\|^2 + \sigma_{3j}\left\|m_{0j}\right\|^2 + \sigma_{4j}\left\|w_{cj}\right\|^2\right\},$$

which implies that V, $\dot{V} \in L_\infty$, and therefore $\mathbf{S}$, $\dot{\mathbf{S}}$, $\mathbf{e}$, $\dot{\mathbf{e}}$, $\tilde{\mathbf{K}}_0$, $\tilde{\mathbf{B}}_0$, $\tilde{\mathbf{M}}$, $\tilde{\mathbf{w}}_c \in L_\infty$. Lastly, we can further show that $\left\|\mathbf{e}(t)\right\|$ will converge to a residual set whose size is in the order of $\max\left\{\varepsilon_i, \sigma_{ij}\right\}$ [40].

5.2   Numerical Simulation Results

Here, a result of regulation simulation done by MATLAB is shown in Fig. 5-2, where the designed controller parameters are listed as follows: $\mathbf{\Lambda}_x = 200$, $\mathbf{Q}_x = 130$,

$\mathbf{N}_x = 0.05$, $\Gamma_{1,x} = 70000000$, $\Gamma_{2,x} = 20000$, $\Gamma_{3,x} = 5$, $\Gamma_{4,x} = 20$
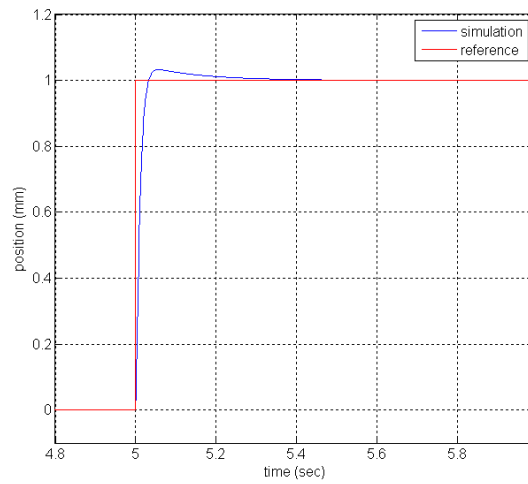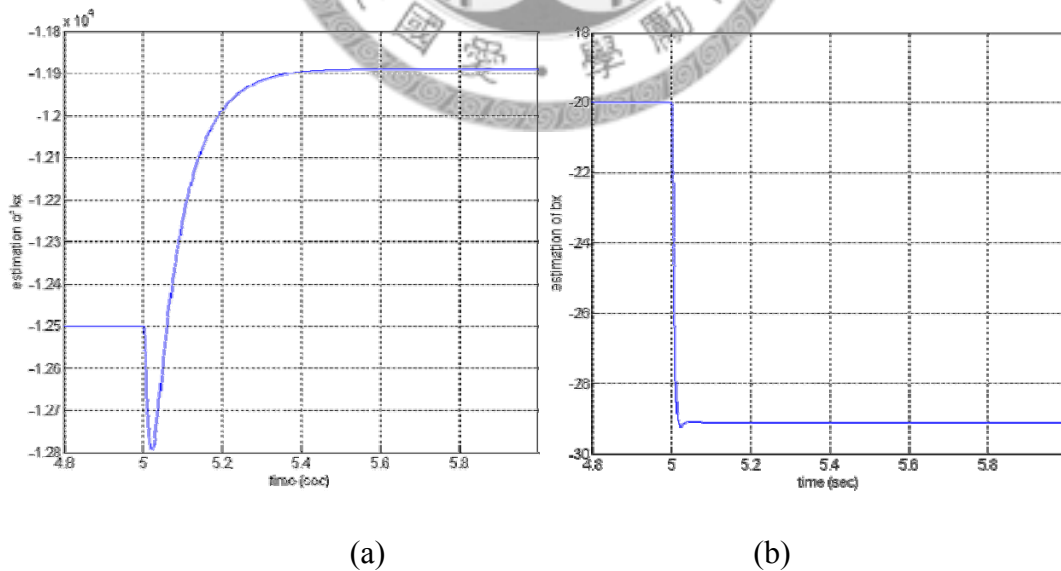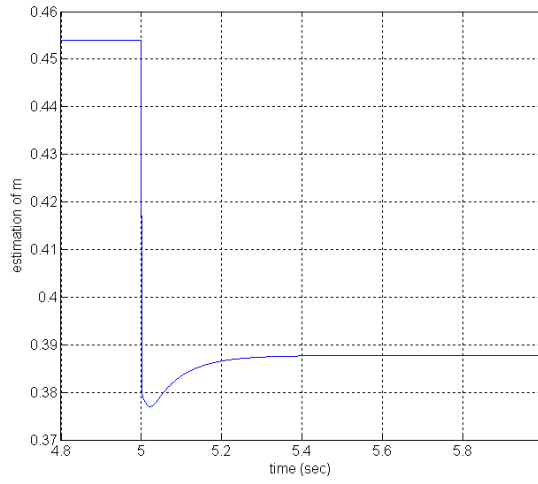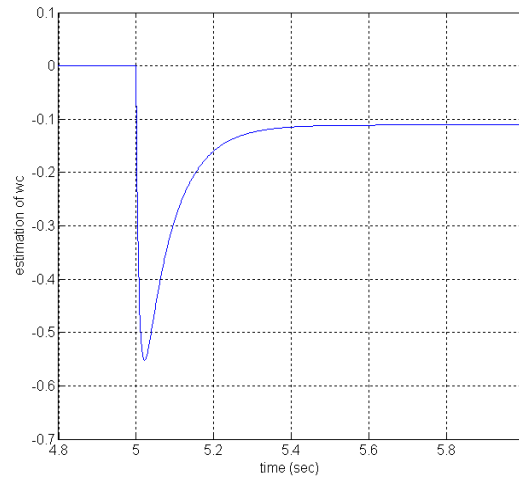
Fig. 5-2 Simulation of adaptive sliding mode controller's regulation.

In Fig. 5-2, it is not hard to find the transient time is within 0.04 seconds. Additionally, this simulation result also reveals that all the estimated signals are converged and bounded as shown in Fig. 5-3. Instead, for convenience, here we only show the first elements of $\hat{\mathbf{K}}_0$, $\hat{\mathbf{B}}_0$, $\hat{\mathbf{M}}_0$, and $\hat{\mathbf{w}}_c$, respectively.
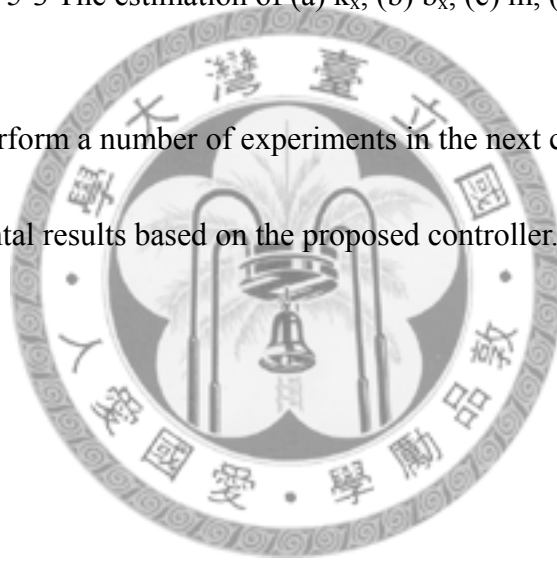

(a)   (b)

Fig. 5-3 The estimation of (a) k_x, (b) b_x, (c) m, (d) w_c

Next, we will perform a number of experiments in the next chapter and meanwhile,

discuss the experimental results based on the proposed controller.

Chapter 6
Experimental Results

6.1 Hardware and Experimental Environment

To make the positioning stage compact and to utilize the advantages of monolithic construction, the flexure mechanism stage is fabricated through precision wire electrical discharge machining (EDM). The width of the flexure is only 0.3mm, which is shown in Fig. 6-1. It also shows the inlaid structure which is mentioned in Section 3.3. The outer frame is made of copper, which is non-ferromagnetic, and the inner movable stage and the flexure are made of steel, which is ferromagnetic. Then the inner flexure is inlaid into the outer copper frame.The overall dimension of the positioning stage is $110 \times 110 \times 35$ mm^3.
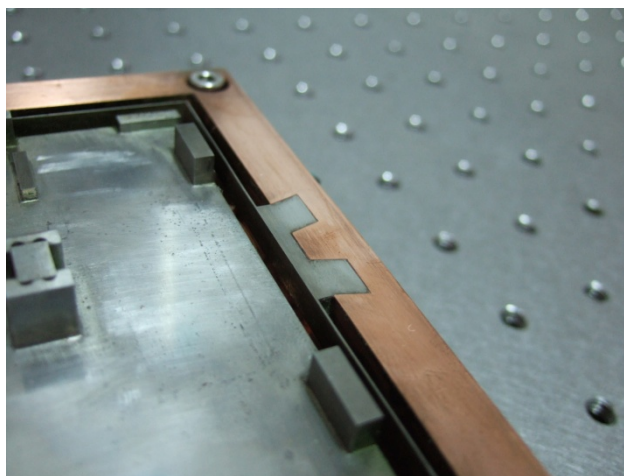
Fig. 6-1 The flexure mechanism and inlaid structure

In order to avoid the electromagnetic interference effect and meet the requirements of long travel range and high resolution, the optical sensors are therefore chosen in our system. They are manufactured by *OMRON*, with 10 *kHz* sampling frequency, 8mm active range, and 10μm accuracy. So far, we have achieved satisfactory performance using this kind of sensors. Figure 6-2 shows the noise of the displacement sensor to measure a static object. The root mean square value of the 10000 sampled data is 2.3μm.
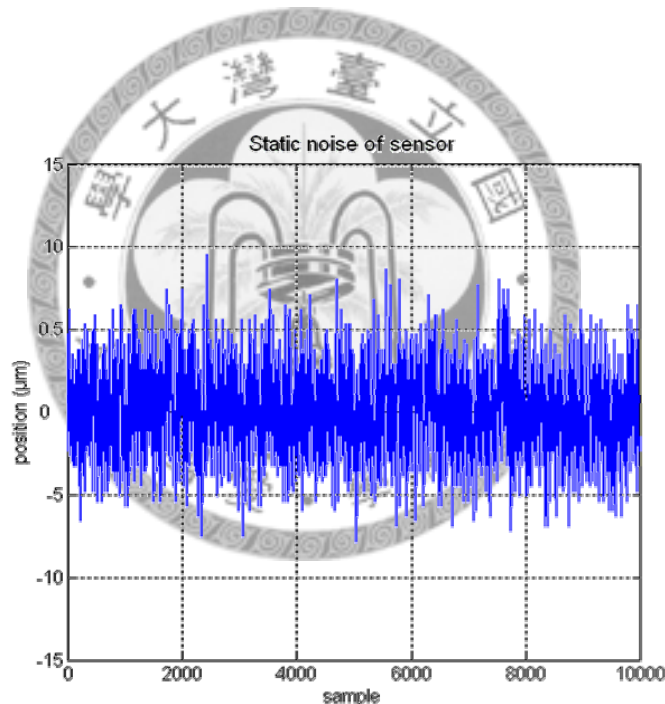

Fig. 6-2 The noise of the displacement sensor

The amplifiers, manufactured by *Copley Controls Corp.*, are linear servo amplifiers for DC brush motors. We use the torque mode to transform the voltage drive into current drive. Table 6-1 lists the specifications of the microcomputer and the used A/D, D/A cards, manufactured by *National Instruments*.

Table 6-1 Specifications of the PC-based controller.

CPU	PentiumIV 2.4 G*Hz*
RAM	512*MB*
Operating System	Windows XP
Language	Matlab Real-Time Windows Target Ver.2.5.1
D/A card	NI 6733 (16 bits)
A/D card	NI 6034E (16 bits)

The software environment is the Matlab Real-Time Windows Target of Version 2.5.1, which is a PC-based solution for real-time application. We can generate executable code with Real-Time Workshop, State-flow Coder, and the C/C++ compiler. Then, we can run the real-time application with "Simulink" in external mode.

The compact positioning stage is shown in Fig. 6-3. The figure also indicates that three displacement sensors are mounted at the side of the positioning stage to measure the position and posture of the stage.
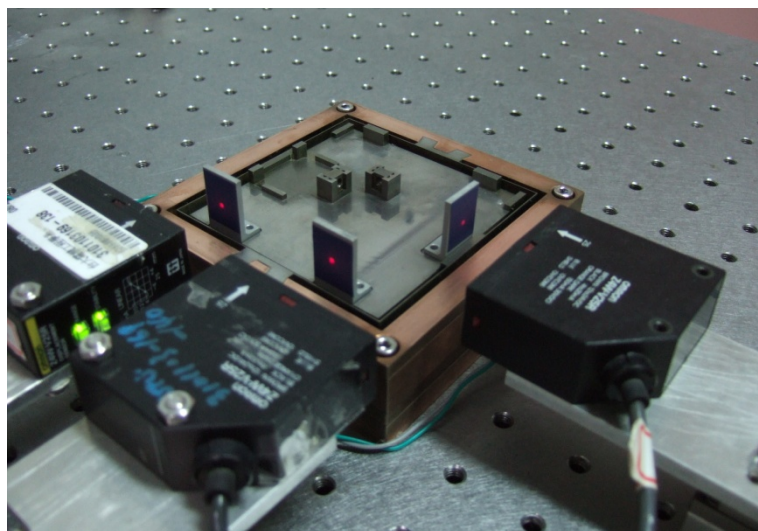

Fig. 6-3 The positioning stage and sensors

6.2 The Vibration Suppression

The vibration of flexure mechanism is a serious challenge to the control of the positioning stage utilizing flexure suspension. In the proposed system, the electromagnetic eddy current damper is used to provide additional damping in this system to attenuate the vibration. Through some simple experiments, the effect of the proposed damper can be easily verified. Figure 6-4 shows open-loop impulse responses of the positioning stage without and with the eddy current damper. The blue curve in Fig. 6-4 indicates the response without the eddy current damper. The vibration takes much longer time to decay than the one of the red line, which indicates the response without eddy current damper. The decay time is shortened from about 17 seconds to 0.8 seconds. The same phenomenon can be found for the case of step response as shown in Fig. 6-5.
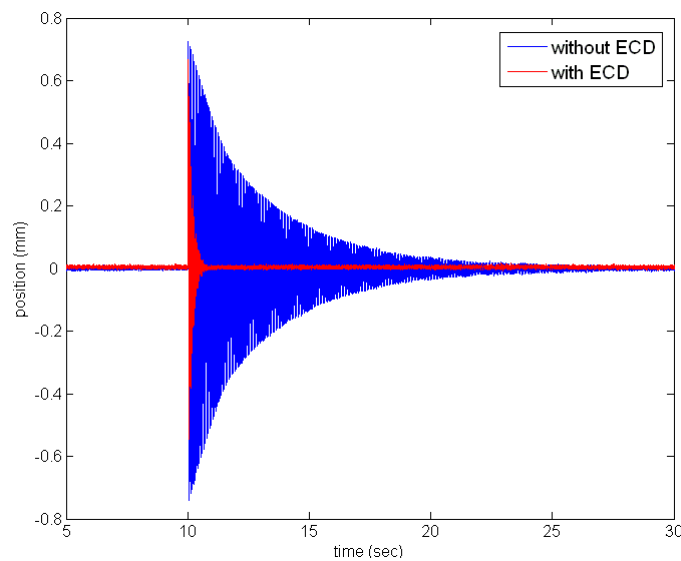

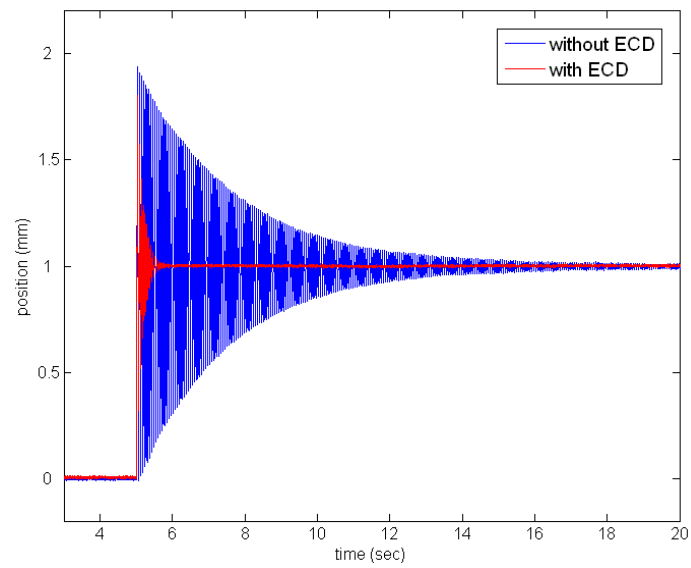Fig. 6-4 The vibration suppression in impulse response

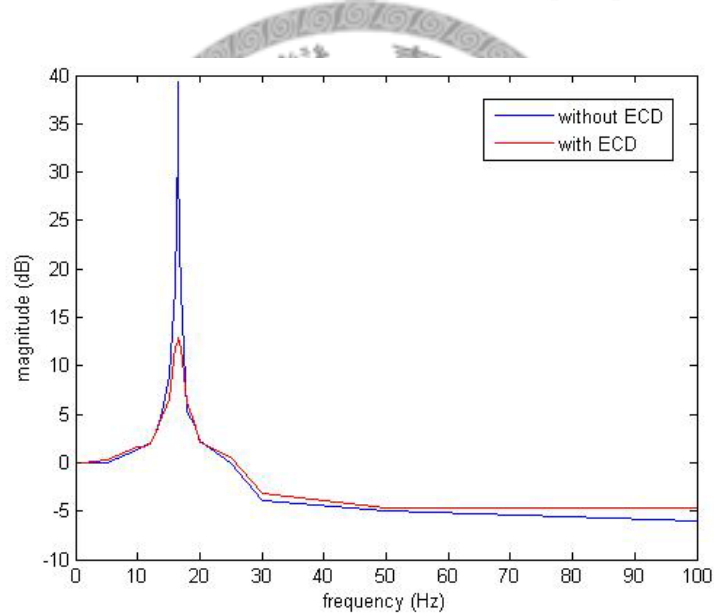Fig. 6-5 The vibration suppression in step response

Fig. 6-6 The vibration suppression in frequency response

Responses in the frequency domain with and without the eddy current damper are shown in Fig. 6-6. The frequency responses from 1Hz to 100Hz are measured and compared. At the natural frequency, 16.5Hz, of the flexure mechanism, the magnitude of response is reduced about 26dB. According to the above three experiments, the vibration can be significantly suppressed by our purposed eddy current damper.

6.3   The Verification of Linear Actuator

The experiment to verify the effectiveness of the design of the linear electromagnetic is designed and shown in Fig. 6-7. The actuator is connected to a load cell and then is fixed on an X-Y-Z positioning stage. The load cell can measure the force exerted by the actuator. The X-Y-Z positioning stage is used to change the position of the movable steel structure relative to the fixed coil mount to check the output force of the actuator at different position.
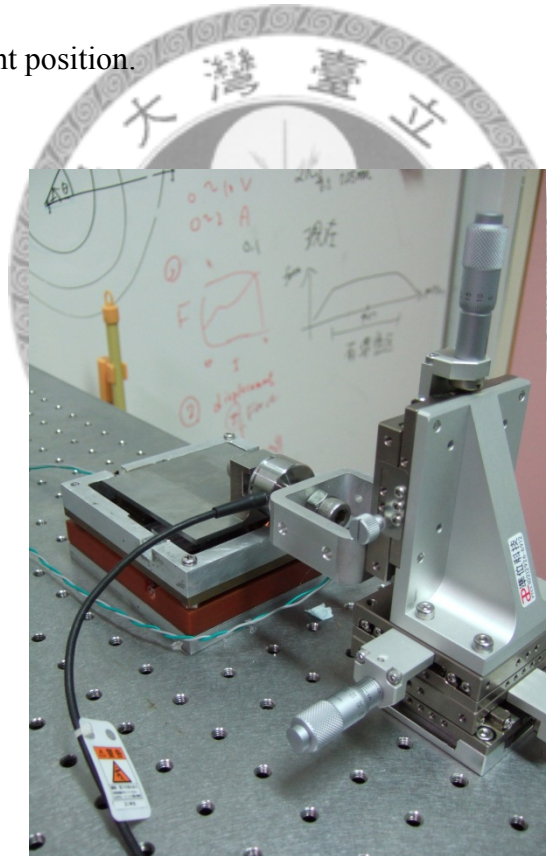

Fig. 6-7 The measurement equipment of the force variation

Figure 6-8 shows the measurement results of the output force on the desired motion plane. The traveling range is 3mm x 3mm. These forces are normalized by

dividing the maximum value. From this figure, the results show that on our desired

traveling plane, the variance of the forces does not exceed 2%. In the view of practical,

the variance can be ignored and the electromagnetic actuator can be regarded as an
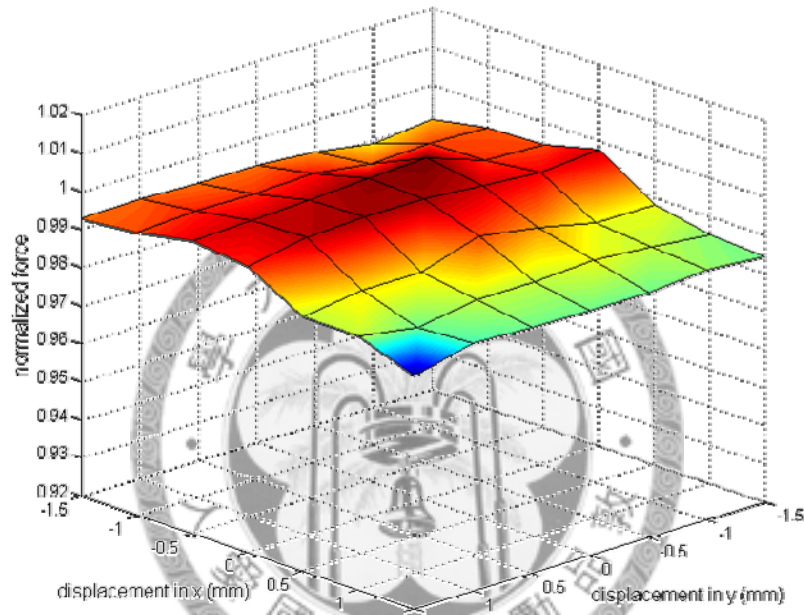
approximated linear actuator.

Fig. 6-8 The variance of the force in the traveling range

6.4   Results of Adaptive Sliding Mode Control

This section shows the experimental results of the adaptive sliding mode control.

The designed parameters are:

$$\mathbf{\Lambda} = \begin{bmatrix} 80 & 0 & 0 \\ 0 & 90 & 0 \\ 0 & 0 & 30 \end{bmatrix} \mathbf{Q} = \begin{bmatrix} 120 & 0 & 0 \\ 0 & 130 & 0 \\ 0 & 0 & 40 \end{bmatrix} \mathbf{N} = \begin{bmatrix} 0.005 & 0 & 0 \\ 0 & 0.005 & 0 \\ 0 & 0 & 0.001 \end{bmatrix}$$

$$\Gamma_1 = \begin{bmatrix} 6\times10^8 & 0 & 0 \\ 0 & 5\times10^8 & 0 \\ 0 & 0 & 5\times10^8 \end{bmatrix} \Gamma_2 = \begin{bmatrix} 10^5 & 0 & 0 \\ 0 & 10^5 & 0 \\ 0 & 0 & 10^5 \end{bmatrix} \Gamma_3 = \begin{bmatrix} 20 & 0 & 0 \\ 0 & 30 & 0 \\ 0 & 0 & 20 \end{bmatrix}$$

$$\Gamma_4 = \begin{bmatrix} 600 & 0 & 0 \\ 0 & 500 & 0 \\ 0 & 0 & 100 \end{bmatrix}$$

6.4.1 Step and regulation response

Step and regulation responses are shown here in order to test the dynamic property and the positioning precision of the positioning stage. Figure 6-9 shows the measured data of the step response, where at $t = 5$, a step command is given to the stage. Fig. 6-10 shows the transient response, where the rise time is 65ms (from 0 to 98% of the step size), there is no overshoot, and the settling time is 70ms.
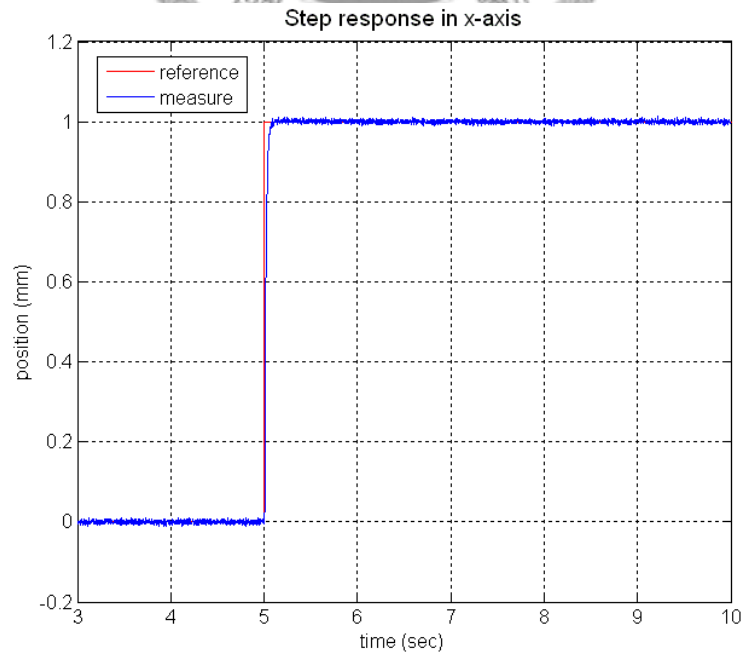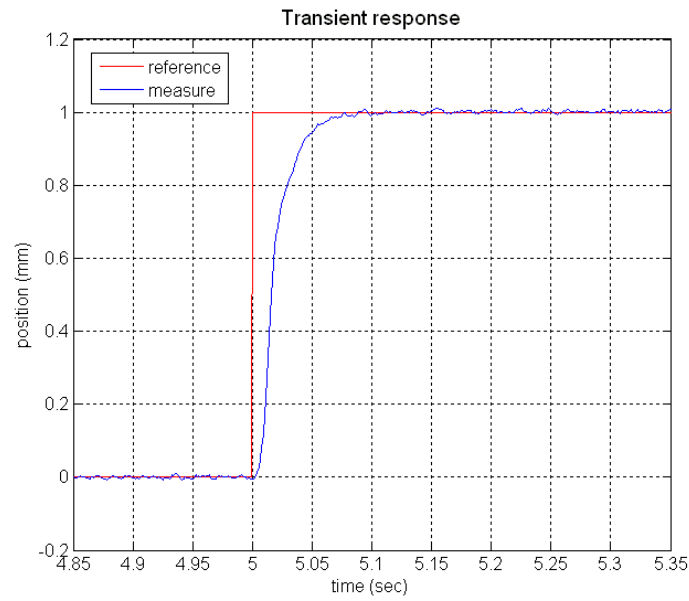

Fig. 6-9 1mm step response on X-axis

88

Fig. 6-10 The transient of the step response

The steady state error is shown in Fig. 6-11. The root mean square value of the error is 3.25μm, which is close to the limit of the sensors used in the system. The other two states, y and θ, are shown in Fig. 6-12. The unexpected couplings in the other axes are not serious.
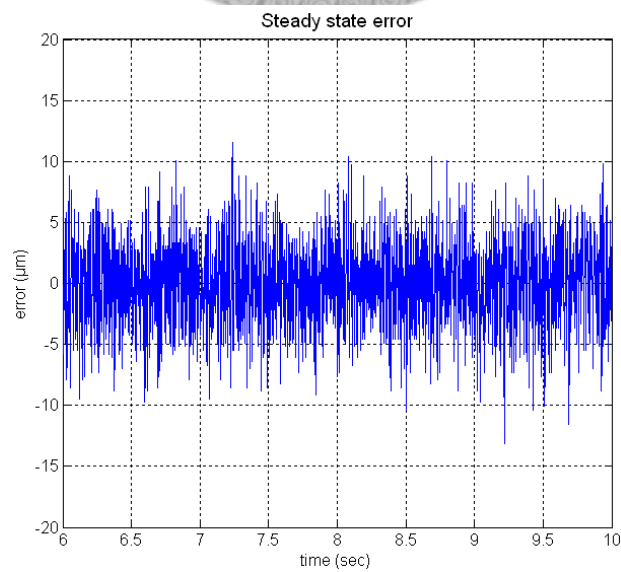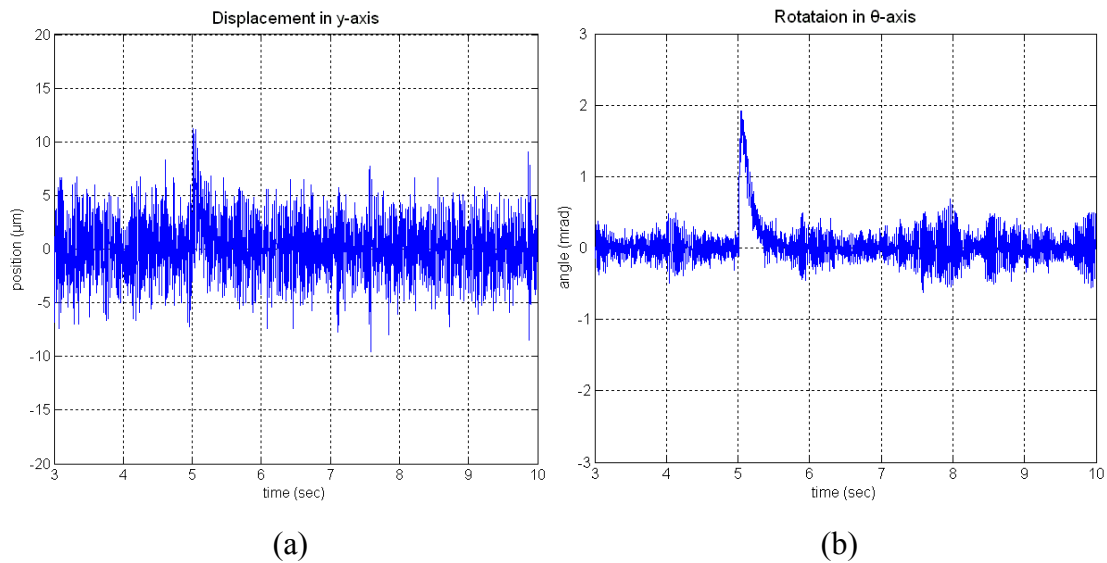

Fig. 6-11 The steady state of step response

Fig. 6-12 The remainder states of step response, (a) displacement in y-axis, and (b) rotation in θ-axis

6.4.2 Sinusoidal tracking response

Figure 6-13 shows experimental result of the sinusoidal tracking with 1mm sinusoidal amplitude at the frequency 0.5Hz along the x-axis. The experimental result shows the fine tracking ability, with both tiny positioning error and little time delay. Figure 6-14 shows the tracking error. Notice that due to the modeling error, the tracking error is large at the beginning. With the adaptive law to on-line estimate system parameters and tune the gain of the sliding mode controller to more adequate values, the tracking error decrease with time. The root mean square value of the tracking error from 15 seconds to 20 seconds is only 10.6μm. Figure 6-15 shows the other two states of the positioning system.
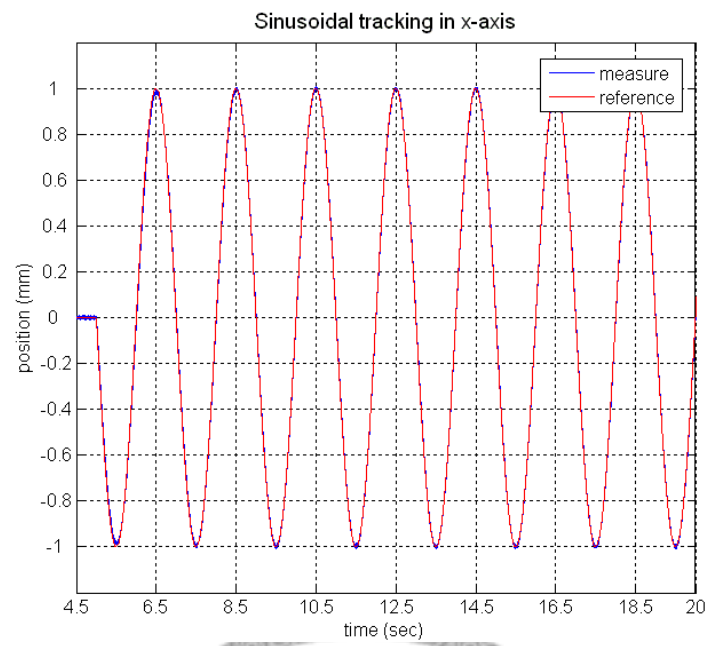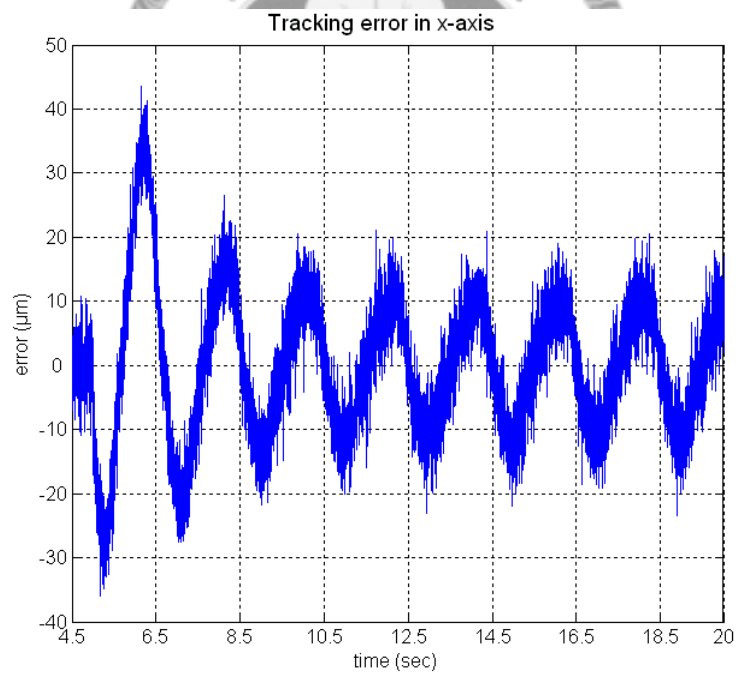
Fig. 6-13 0.5Hz sinusoidal tracking in x-axis

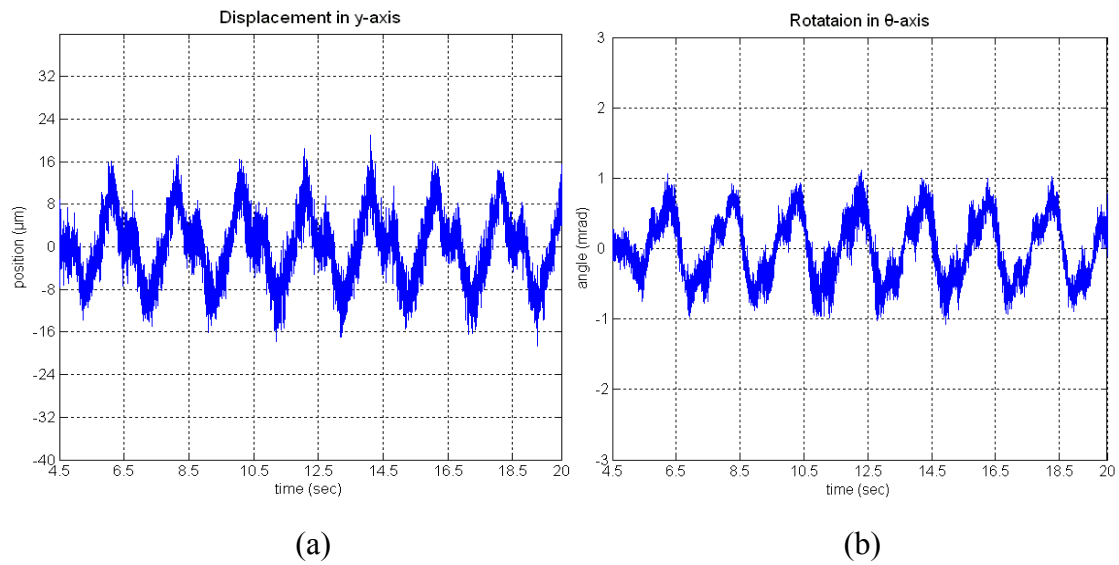

Fig. 6-14 Sinusoidal tracking error

(a)   (b)

Fig. 6-15 The remainder states of sinusoidal tracking, (a) displacement in y-axis, and (b) rotation in θ-axis

6.4.3   Circular contouring

The other way to show the tracking capability is to profile a desired contour. In the experiment of this section, a circle which radius equal to 1mm is our desired reference contour, and the frequency of circling is 0.5Hz. Figure 6-16 shows the tracking trajectory of the positioning stage between 20 seconds and 30 seconds. The root mean square value of the tracking error shown in Fig. 6-17 is 23.1μm.
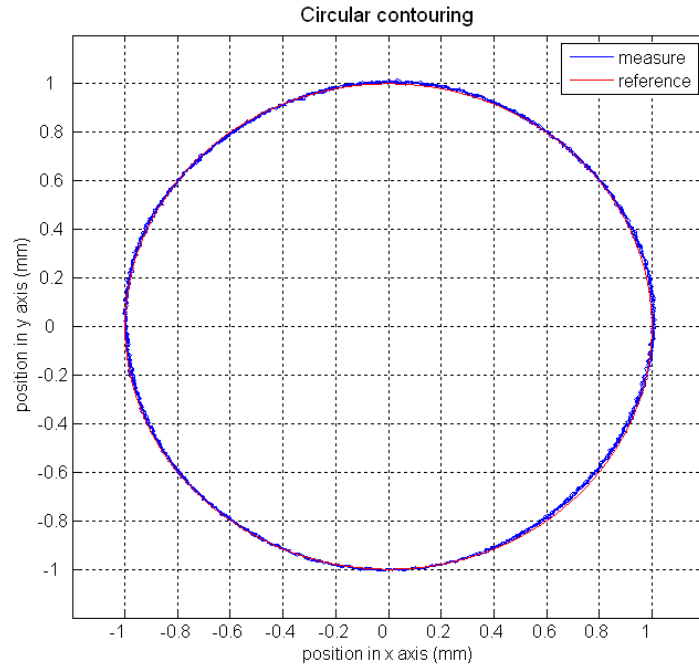
92

Fig. 6-16 Trajectory of circular contouring
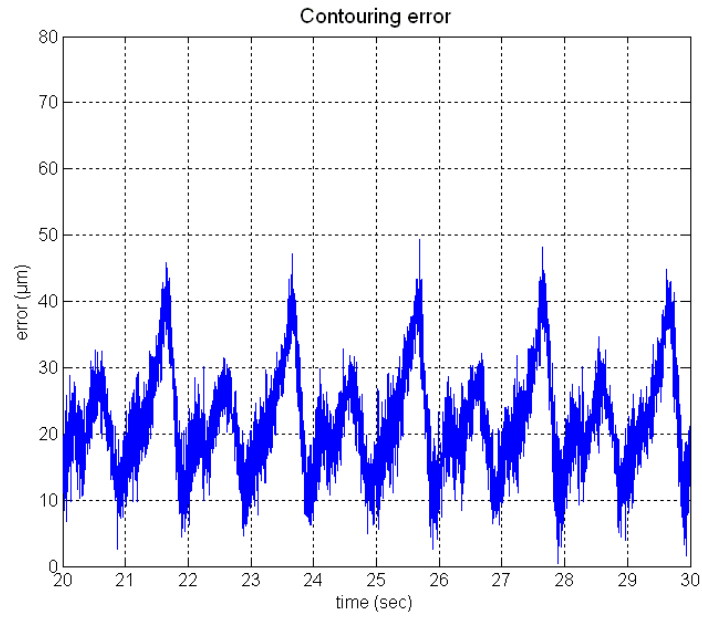

Fig. 6-17 Contouring error of circular motion

6.4.4   Spiral motion

In one of the future applications of the proposed positioning stage, atomic force

microscope (AFM), the spiral scanning is useful to replace the conventional raster

scanning in order to avoid the high acceleration at the sharp turn [41]. In the section, the experimental result of the spiral motion is shown to verify the capability of the proposed positioning stage serving as the scanner of AFM. Figure 6-18 shows the tracking trajectory. The reference spiral curve starts at the origin and then increase the radius with time. The velocity is designed as a constant to keep the motion smooth. The tracking error is shown in Fig. 6-19, and the root mean square value of the tracking error is 8μm.
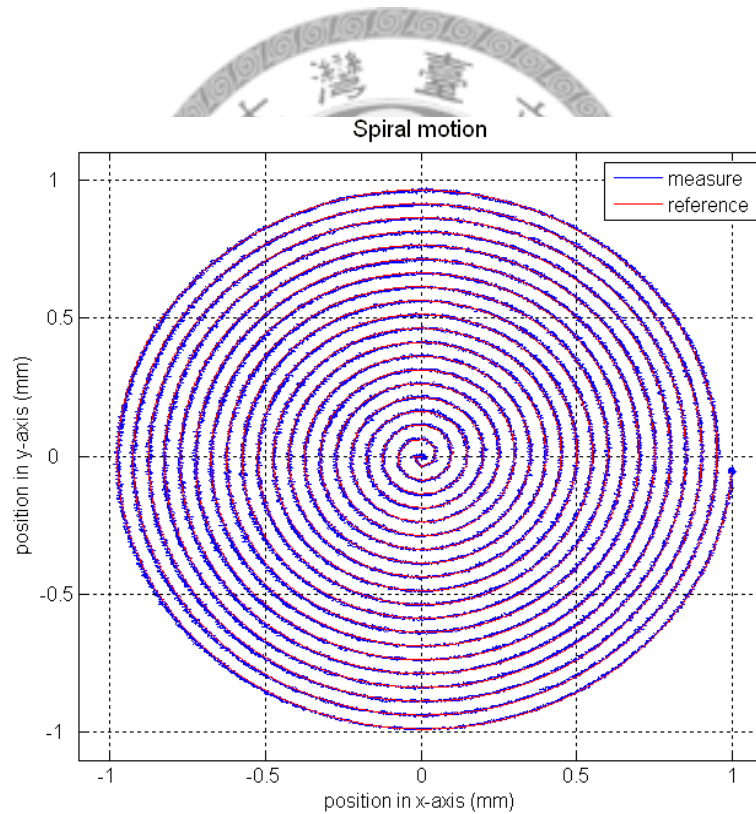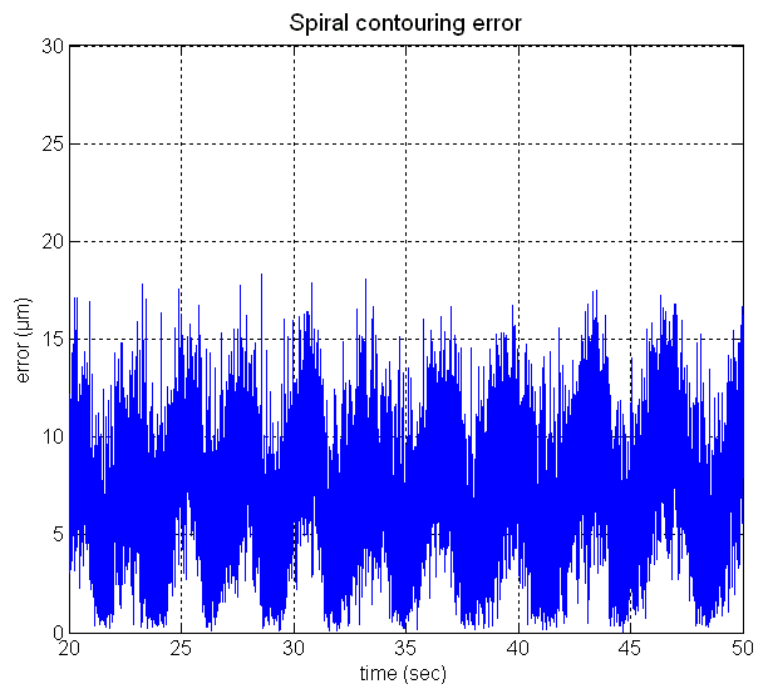

Fig. 6-18 Trajectory of spiral contouring

Fig. 6-19 Contouring error of spiral motion

Chapter 7
Conclusions

In this thesis, we have first surveyed several kinds of research results relevant to the current precision positioning techniques, especially for the positioning utilizing flexure mechanism. Then, we have designed and implemented a precision positioning stage utilizing parallel flexure mechanism, electromagnetic actuator, and damper. This proposed system consists of frictionless flexure mechanism as the guidance, linear electromagnetic actuators to generate the desired 3-DOF motion, noncontact eddy current damper to suppress the vibration of the flexure structure. Three optical displacement sensors are used to obtain the present position and posture of the stage. The positioning stage possesses smooth linear motion capability by involving only pure and linear magnetic forces.

Next, the dynamics of our 3-DOF positioning system has been thoroughly analyzed and its mathematical model with complete three DOFs has also been detailed derived. After that, an advanced adaptive sliding-mode controller is designed and implemented in a personal computer to regulate the three DOFs up to a precision level and to track a particular desired trajectory.

Finally, satisfactory performance of the precision positioning motion can be obtained in the actual experiments. The travel range of this proposed positioning stage is 3mm×3mm with the accuracy close to the limit of the sensor. Furthermore, based on the adaptive sliding-mode controller, the system's response is also fast enough. Several experimental results show that the adaptive sliding-mode controller has satisfactory performance of the robustness when dealing with uncertainties and disturbances. The successful performances of the linear actuator and noncontact electromagnetic damper are also revealed by the experimental results. As a consequence, various goals which are set in the beginning of the thesis have been successfully fulfilled. To sum up, a novel 3-DOF high-precision compact positioning stage has been successfully brought to practice in this thesis.
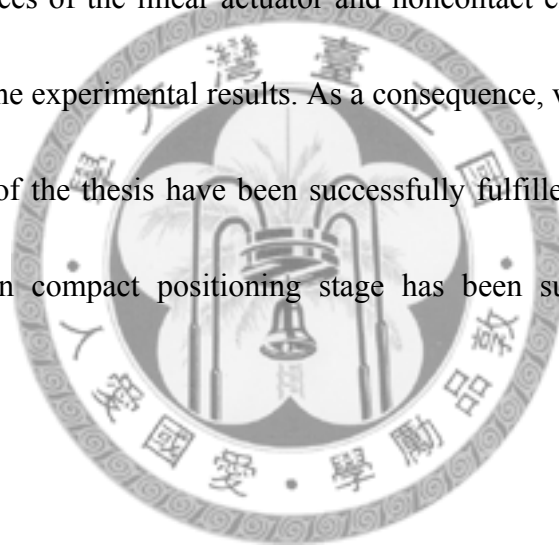
Reference

[1] S. Devasia, E. Eleftheriou, and S. O. R. Moheimani, "A survey of control issues in nanopositioning," *IEEE Transactions on Control Systems Technology,* vol. 15, pp. 802-23, 2007.

[2] G. Binnig, C. F. Quate, and C. Gerber, "Atomic force microscope," *Physical Review Letters,* vol. 56, pp. 930-3, 1986.

[3] S. Salapaka, A. Sebastian, J. P. Cleveland, and M. V. Salapaka, "High bandwidth nano-positioner: A robust control approach," *Review of Scientific Instruments,* vol. 73, p. 3232, 2002.

[4] M. Sitti and H. Hashimoto, "Controlled pushing of nanoparticles: modeling and experiments," *IEEE/ASME Transactions on Mechatronics,* vol. 5, pp. 199-211, 2000.

[5] S. Verma, W.-J. Kim, and H. Shakir, "Multi-axis maglev nanopositioner for precision manufacturing and manipulation applications," *IEEE Transactions on Industry Applications,* vol. 41, pp. 1159-1167, 2005.

[6] H. Brian Armstrong, louvry, D. Pierre, and W. Carlos Canudas de, "A survey of models, analysis tools and compensation methods for the control of machines with friction," *Automatica,* vol. 30, pp. 1083-1138, 1994.

[7] J. Swevers, F. Al-Bender, C. G. Ganseman, and T. A. P. T. Projogo, "An integrated friction model structure with improved presliding behavior for accurate friction compensation," *IEEE Transactions on Automatic Control,* vol. 45, pp. 675-686, 2000.

[8] 黃宣翰, "Design and Implementation of a New 3-DOF Electromagnetic-Nanopositioner Utilizing Flexure Mechanism." Master thesis. The National Taiwan University, Taiwan, R.O.C., 2005.

[9] 吳兆開, "A Novel 6-DOF Electromagnetic Precision Positioner Utilizing Flexure Mechanism," Master thesis. The National Taiwan University, Taiwan, R.O.C., 2006.

[10] S.T. Smith, *Flexures: Elements of Elastic Mechanisms*, Gordon & Breach, Amsterdam, 2000

[11] S. Salapaka, "Control of the Nanopositioning Devices," in *Proc. of Conference on Decision and Control*, 2003.

[12] S. H. Chang, C. E. Tseng, and H. C. Chien, "An ultra-precision $XY\theta_Z$ piezo micropositioner Part I: Design and analysis," in *IEEE Transactions on Ultrasonic, Ferroelectric, and Frequency Control*, Vol.46, no.4, pp.897-905, Jul. 1999.

[13] B. J. Yi, G. B. Chung, H. Y. Na, W. K. Kim, and I. H. Suh, "Design and Experiment of a 3-DOF Parallel Micromechanism Utilizing Flexure Hinges," in *IEEE Trans. on Robotics and Automation*, Vol.19, no.4, 2003

[14] S. Awtar, "Synthesis and Analysis of Parallel Kinematic XY Flexure Mechanisms," Ph. D. Dissertation, Dept. Mech. Eng., Massachusetts Institute of Technology, Cambridge, MA, Feb. 2004.

[15] Y. Li and Q. Xu, "A Novel Design and Analysis of a 2-DOF Compliant Parallel Micromanipulator for Nanomanipulation", *IEEE Transactions on Automation Science and Engineering*, Vol. 3, No. 3, pp. 247－254, July 2006.

[16] Q. Yao, J. Dong, P.M. Ferreira, "Design, analysis, fabrication and testing of a parallel-kinematic micropositioning XY stage," International Journal of Machine Tools & Manufacture, Vol. 47, p.p. 946－961, 2007

[17] R. C. Hibbeler, "*Mechanics of Materials*," Fourth edition, Prentice Hall, 2000.

[18] H. A. Sodano and J. S. Bae, "Eddy Current Damping in Structures," *The Shock and Vibration Digest*, Vol. 36, No. 6, pp. 469–478, Nov. 2004.

[19] J. -S. Bae, M. K. Kwak, D. J. Inman, "Vibration suppression of a cantilever beam using eddy current damper," *Journal of Sound and Vibration*, vol. 284, pp. 805-824, June 2005.

[20] Products P-280 and P-762, Physik Instrumente Product Catalog, 2001, MicroPostioning, NanaoPositioning, NanoAutomation: Solutions for Cutting-Edge Technologies

[21] F. L. Fischer, 1981, "Symmetrical 3 DOF Compliance Structure", US Patent 4447048

[22] A. R Smith., S. Gwo, and C. K. Shih, "A new high resolution two-dimensional micropositioning device for scanning probe microscopy", *Review of Scientific Instruments*, Vol. 64, no. 10, pp 3216-3219, 1994

[23] N. G. Dagalakis, J. A. Kramer, E. Amatucci, R. Bunch, "Kinematic Modelling and Analysis of Planer Micro-positioner", in *Proceedings of ASPE Annual Meeting*, pp 135-138, 2001

[24] "Agilent Technologies NanoStepper", MIT Technology Review, pp. 14. June 2003.

[25] J. G. Bednorz., et al, 1985, Piezoelectric XY Positioner, US Patent 452 0570

[26] J. W. Ryu, D. G. Gweon, and K. S. Moon., "Optimal Design of a Flexure hinge based X-Y-θ wafer stage", *Journal of Precision Engineering*, Vol.21 no.1, pp 18-28, 1997

[27] T. B. Eom and J. Y. Kim, "Long Range Stage for the Metrological Atomic Force Microscope", in *Proceedings of ASPE 2001 Annual Meeting*, pp. 156-159, 2000

[28] Kanai et al, "An Elastic Fine Positioning Mechanism Applied to Contactless X-Y Table", *Bulletin of JSPE*, Vol 17, no. 4, pp 265-266, 1983

[29] J. N. Juang, "*Applied System Identification*," Amazon.com, 1993.

[30] L. Ljung, "*System identification : Theory for the user*," Upper Saddle River, NJ : PTR Prentice Hall, 2nd edition, 1999.

[31] D. Guang-Ren, W. Zhan-Yuan, B. Chris, and H. David, "Robust magnetic bearing control using stabilizing dynamical compensators," *IEEE Transactions on Industry Applications,* vol. 36, pp. 1654-1660, 2000.

[32] D. Guang-Ren and D. Howe, "Robust magnetic bearing control via eigenstructure assignment dynamical compensation," *IEEE Transactions on Control Systems Technology,* vol. 11, pp. 204-215, 2003.

[33] S. Peng and S. Shyh-Pyng, "Robust H∞ control for linear discrete-time systems with norm-bounded nonlinear uncertainties," *IEEE Transactions on Automatic Control,* vol. 44, pp. 108-111, 1999.

[34] K. Oui-Serg, L. Sang-Ho, and H. Dong-Chul, "Positioning performance and straightness error compensation of the magnetic levitation stage supported by the linear magnetic bearing," *IEEE Transactions on Industrial Electronics,* vol. 50, pp. 374-378, 2003.

[35] X. Yuanqing and J. Yingmin, "Robust sliding-mode control for uncertain time-delay systems: an LMI approach," *IEEE Transactions on Automatic Control,* vol. 48, pp. 1086-1091, 2003.

[36] M. Torres, H. Sira-Ramirez, and G. Escobar, "Sliding mode nonlinear control of magnetic bearings," *Proceedings of the IEEE International Conference on Control Applications,* vol. 1, pp. 743-748, 1999.

[37] S. L. Edmond and J. K. Pieper, "Discrete sliding mode control of magnetic bearings," *Proceedings of the IEEE International Conference on Control Applications,* pp. 658-663, 2000.

[38] H. Sung-Kyung and R. Langari, "Robust fuzzy control of a magnetic bearing system subject to harmonic disturbances," *IEEE Transactions on Control Systems Technology,* vol. 8, pp. 366-371, 2000.

[39] K. Ki-Seok and K. Youdan, "Robust backstepping control for slew maneuver using nonlinear tracking function," *IEEE Transactions on Control Systems Technology,* vol. 11, pp. 822-829, 2003.

[40] P.A. Ioannou, and J. Sun, "*Robust Adaptive Control,*" Prentice Hall, 1998.

[41] 洪紹剛, "Design and Control of Novel Atomic Force Microscope Systems," Ph.D. Dissertation. The National Taiwan University, Taiwan, R.O.C., 2007.